



JGR Solid Earth

RESEARCH ARTICLE

10.1029/2024JB029346

Key Points:

- We developed a coupling zone boundary inversion with a forward model of shallow creep at constant stress and deep updip-propagating creep.
- The locked zone accounts for 48% of the interseismic moment accumulation rate at Cascadia and 46% at Nankai
- We infer steep creep rate gradients, indicative of updip-propagating creep, at Cascadia and below Shikoku and Shima peninsula at Nankai

Supporting Information:

Supporting Information may be found in the online version of this article.

Correspondence to:

E. M. Sherrill, sherrile@iu.edu

Citation:

Sherrill, E. M., Johnson, K. M., & Jackson, N. M. (2024). Locating boundaries between locked and creeping regions at Nankai and Cascadia subduction zones. *Journal of Geophysical Research: Solid Earth*, 129, e2024JB029346. https://doi.org/10.1029/2024JB029346

Received 17 APR 2024 Accepted 16 OCT 2024

Author Contributions:

Conceptualization: K. M. Johnson, N. M. Jackson

Data curation: E. M. Sherrill,

K. M. Johnson

Formal analysis: E. M. Sherrill,

K. M. Johnson

Funding acquisition: K. M. Johnson,

N. M. Jackson

Investigation: E. M. Sherrill,

K. M. Johnson

Methodology: E. M. Sherrill, K. M. Johnson, N. M. Jackson

Project administration: K. M. Johnson,

N. M. Jackson

Software: E. M. Sherrill, K. M. Johnson **Supervision:** K. M. Johnson,

N. M. Jackson

Validation: E. M. Sherrill, K. M. Johnson Visualization: E. M. Sherrill.

K. M. Johnson

Writing – original draft: E. M. Sherrill, K. M. Johnson

© 2024. American Geophysical Union. All Rights Reserved.

Locating Boundaries Between Locked and Creeping Regions at Nankai and Cascadia Subduction Zones

E. M. Sherrill¹, K. M. Johnson¹, and N. M. Jackson²

¹Department of Earth and Atmospheric Sciences, Indiana University, Bloomington, IN, USA, ²Department of Geology, University of Kansas, Lawrence, KS, USA

Abstract Interseismic coupling maps and, especially, estimates of the location of the fully coupled (locked) zone relative to the trench, coastline, and slow slip events are crucial for determining megathrust earthquake hazard at subduction zones. We present an interseismic coupling inversion that estimates the locations of the upper and lower boundaries of the locked zone, the lower boundary of the deep transition zone, and downdip gradient of creep rate in the transition from locked to freely creeping in the downdip transition zone. We show that the locked zone at Cascadia is west of the coastline and 10 km updip of the slow slip zone along much of the margin, widest (25–125 km, extending to ~19 km depth) in northern Cascadia, narrowest (0–70 km) in central Cascadia, with moment accumulation rate equivalent to a M_w 8.71 and M_w 8.85 earthquake for 300- and 500-year earthquake cycles. We find a steep gradient in creep immediately below the locked zone, indicative of propagating creep, along the entire margin. At Nankai, we find three distinct zones of locking (offshore Shikoku, offshore southeast Kii peninsula, and offshore Shima peninsula) with a total moment accumulation rate equivalent to a M_w 8.70 earthquake for a 150-year earthquake cycle. The bottom of the locked zone is nearly under the coastline for all three locked regions at Nankai and is positioned 0–5 km updip of the slow slip zone. In contrast with Cascadia, creep rate gradients below the locked zone at Nankai are generally gradual, consistent with stationary locking.

Plain Language Summary Maps of where faults are not moving (the locked zone) can be used to assess future earthquake size and impacts on nearby communities due to ground shaking and tsunamis. Slow slip events, occurring below and around the locked zone, may transfer stress from deeper on the fault to the locked zone and increase earthquake potential. We use measurements of movement of the surface of the earth and models of how surface movements reflect to slip on a fault in order to locate the boundaries of the locked zone in relation to the coastline, the trench, and slow slip events at Cascadia and Nankai subduction zones. We find that a release of slip accumulated in the current Cascadia and Nankai locked zones would result in earthquakes of magnitude M_w 8.71–8.85 and M_w 8.70, respectively. We also find evidence that the depth to the bottom edge of the locked zone at Cascadia and in some areas of Nankai may have shallowed since the last earthquake. Our model provides better estimates and realistic ranges for the location of the boundaries of the locked zone which can inform earthquake rupture, ground motion, and tsunami models.

1. Introduction

Gradual strain accumulation due to the convergence of two tectonic plates can be detected by geodetic observations and modeled to obtain a map of interseismic coupling – the degree to which the fault is not keeping up with the plate convergence rate between earthquakes. Coupling is the ratio of the interseismic creep rate to the plate rate and ranges from zero (fully creeping or slipping at the plate convergence rate) to one (fully coupled or locked). Interseismic coupling maps are integral for megathrust earthquake hazard assessment because locked areas, sometimes referred to as asperities, are expected to slip in earthquakes (e.g., Chlieh et al., 2008; Loveless & Meade, 2010; Metois et al., 2016; Moreno et al., 2010; Nocquet et al., 2017). The overall size of the highly coupled areas, together with the slip rate and time since the last earthquake, provides a rough estimate of the moment available to be released in future earthquakes. Estimation of the updip extent of the locked areas is critical for estimating the tsunamigenic potential of a future earthquake but is often poorly resolved due to a paucity of observations in the offshore area. Crucial for determining megathrust earthquake hazard, the better-resolved downdip edge of high coupling is often used as a proxy for how far inland (and thus how close to population centers) an earthquake can rupture (e.g., Melgar et al., 2022; Petersen et al., 2020; Wirth & Frankel, 2019).

SHERRILL ET AL. 1 of 21



Journal of Geophysical Research: Solid Earth

10.1029/2024JB029346

Writing – review & editing: E. M. Sherrill, K. M. Johnson, N. M. Jackson Differences in coupling models can result in major variations in estimates of potential earthquake shaking and seismic risk to populated areas (e.g., Melgar et al., 2022).

Recent advances in continuous geodetic monitoring have illuminated a spectrum of slip transients occurring at subduction zones, which contribute to the slip budget of the partly coupled regions of the fault. Most notably, at the Nankai and Cascadia subduction zones there is a band of episodic tremor and short-term (days to weeks) slow slip events (S-SSEs), known as the ETS zone, which is located downdip of the locked zone (Figure 1, e.g Obara, 2002; Rogers & Dragert, 2003). The ETS zone has been previously interpreted as delineating the velocity-weakening to velocity-strengthening transition which should correspond to the coupling transition from fully coupled to fully creeping (e.g., Bürgmann, 2018; Peng & Gomberg, 2010). However, at Cascadia and potentially Nankai, there is a geodetically-inferred gap between the bottom of the locked zone and the ETS zone (e.g., Bartlow, 2020; Bruhat & Segall, 2017; Sherrill & Johnson, 2021). Gao and Wang (2017) suggested that the gap may be a velocitystrengthening zone separating the velocity-weakening seismogenic zone updip and a downdip frictional-viscous creeping ETS zone. The location of the ETS zones in Cascadia and Nankai is now thought to be controlled by the presence of high pore fluid pressures (e.g., Behr & Bürgmann, 2021; Hyndman et al., 2015; Shelly et al., 2006). While the gaps at both Nankai and Cascadia are void of large earthquakes and S-SSEs, a number of studies infer long-term (months to years) slow slip events (L-SSEs) and/or coupling changes in the gap (e.g., Hirose et al., 2010; Materna et al., 2019; Nuyen & Schmidt, 2021; Takagi et al., 2016). Very-low frequency earthquakes (VLFEs), thought to be a seismic manifestation of slow slip, have also been located in the gap at Cascadia and the shallow, partly coupled regions of Nankai and Cascadia (e.g., Chaudhuri & Ghosh, 2022; Fan et al., 2022; Ghosh et al., 2015; Takemura et al., 2019).

It is important to understand how stress due to slip during SSEs is transferred updip (Wech & Creager, 2011) because numerical models suggest that SSEs are capable of loading the locked zone and eventually evolving into dynamic rupture (Matsuzawa et al., 2010; Segall & Bradley, 2012). There are no observations of deep SSEs evolving into an earthquake, but there are inferences of shallow SSEs prior to megathrust rupture (Ito et al., 2013; Ruiz et al., 2017; Uchida et al., 2016). If the top of the ETS zone is at the bottom of the locked zone, megathrust earthquake hazard may be higher during times of active S-SSEs, particularly if S-SSEs are migrating updip, whereas a gap between the ETS zone and the locked zone might provide a buffer inhibiting direct stress transfer between S-SSEs and the locked zone. In addition to understanding the spatial relation of the locked and ETS zones, elucidating how creep transitions from fully coupled to fully creeping below the locked zone may provide insights into how stress is being transferred to the locked zone.

It is difficult to extract the boundaries between locked and creeping areas on faults from inversions of geodetic data because interseismic coupling inversions require some sort of regularization and therefore have limited resolution. Some inversions enforce a linear creep rate gradient explicitly (e.g., Schmalzle et al., 2014) or implicitly with spatial smoothing constraints (e.g., Yokota et al., 2016), which favors smooth slip distributions that may be broader than actual transition zones and may underestimate the area of the fault that is locked. Bruhat and Segall (2017) examined physically constrained interseismic coupling in northern Cascadia assuming a locked zone above a transitional creep zone modeled with elastic crack solutions. In their model, the boundary between the locked zone and the deep transitional creep zone is allowed to propagate updip over time, resulting in a rapid transition from locked to fully creeping (steep gradient in creep rate) at the bottom of the locked zone and resulting in a largely creeping gap between the locked zone and the ETS zone. Wang et al. (2003) also proposed a similar model, a wide transition zone with exponentially decreasing slip deficit, but explained it as a way to account for some viscoelastic effects (e.g., stress relaxation in the mantle wedge) with an elastic model. Bruhat and Segall (2017) interpreted the steep gradient as an indication of a propagating creep front and suggested, as did Wang et al. (2003), that the locked zone is not static throughout the interseismic period. Recent inferences of creep and slip transients invading previously locked regions of the faults lend support to this idea (e.g., Kano et al., 2019; Mavrommatis et al., 2015; Ruiz et al., 2017).

To improve resolution of geodetic slip inversions, it is helpful to provide additional constraints on interseismic slip, for example, constraints on stress. Coupling studies for faults around the world show that locked (or very highly coupled) areas of the fault can restrict the creep rates on surrounding areas by casting stress shadows (regions of reduced shear stressing rates), which results in a wide area of partial coupling accumulating slip deficit (Almeida et al., 2018; Bürgmann et al., 2005; Herman et al., 2018; Johnson & Fukuda, 2010; Wang & Dixon, 2004). This realization has encouraged the development of physically constrained interseismic coupling

SHERRILL ET AL. 2 of 21

21699356, 2024, 10, Downloaded from https://agupubs.onlinelibrary.wiley.com/doi/10.10292024JB029346 by Indiana University Libraries, Wiley Online Library on [21/03/2025]. See the Terms and Conditions (https://onlinelibrary.wiley.com/

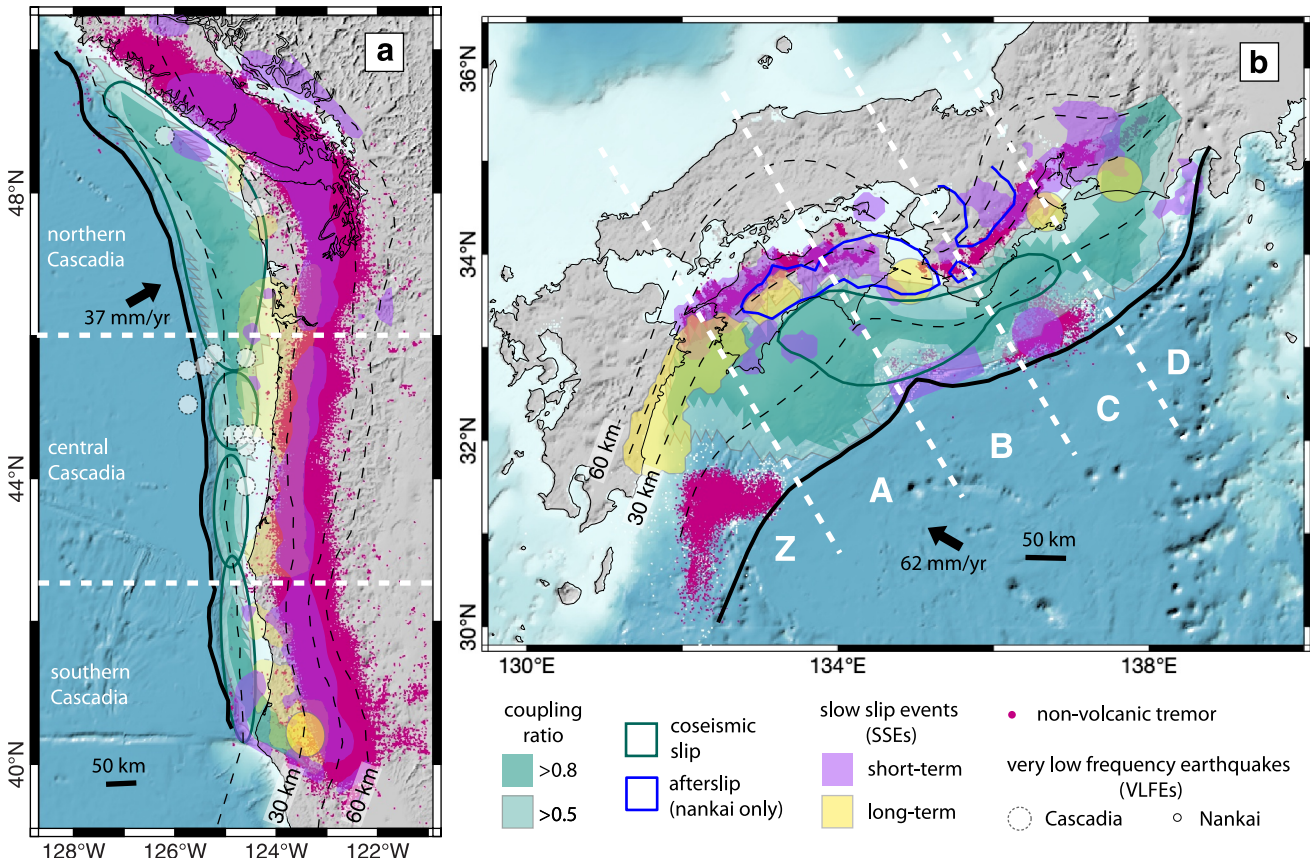


Figure 1. (a) Tectonic setting of Cascadia subduction zone showing median interseismic coupling (this study) in relation to the estimated locations of tremor (Wech, 2021), short-term slow slip events (S-SSEs; Bartlow, 2020), long-term slow slip events (L-SSEs) and dynamic coupling changes (Materna et al., 2019; Nuyen & Schmidt, 2021), very low frequency earthquakes (VLFEs; Chaudhuri & Ghosh, 2022; Fan et al., 2022), and estimated coseismic slip region for the 1700 earthquake (Wang et al., 2013). L-SSEs and VLFEs with relatively small signal are shown with lighter color and dashed boundaries. (b) Tectonic setting of the Nankai subduction zone showing median interseismic coupling (this study) in relation to estimated locations of tremor (Akuhara et al., 2023; Baba et al., 2023; Obara et al., 2010; Yamashita et al., 2015, 2021), S-SSEs (Araki et al., 2017; Kano & Kato, 2020; Yokota & Ishikawa, 2020), L-SSEs (Kobayashi, 2017; Takagi et al., 2016), VLFEs (Akuhara et al., 2023; Takemura et al., 2022), and the inferred coseismic slip and afterslip regions for the 1944/46 earthquakes (Sherrill & Johnson, 2021). Black dashed contour lines represent slab depth at Nankai and Cascadia in 15 km increments (Hayes et al., 2018; Nakanishi et al., 2018). White dashed lines show the regional boundaries for both subduction zones.

inversions with constant stress constraints on creep (e.g., Herman et al., 2018; Johnson, 2013; Johnson et al., 2022; Lindsey et al., 2021; Saito & Noda, 2022). An added benefit to physically constrained inversions, as Lindsey et al. (2021) demonstrated, is the improvement of coupling resolution in the offshore region of the fault where station coverage is limited. One drawback of the constant stress creep models is that they implicitly assume stationary locked areas over time and that creep rate is driven by the rate of steady stress accumulation on the interface. As demonstrated by Bruhat and Segall (2017), if creep propagates into regions of accumulated interseismic stress, the creep rate distribution can vary substantially from the steady creep rate models.

In this study we present an interseismic coupling inversion method that explicitly estimates the boundaries of the locked, shallow transitional creep (STC), and deep transitional creep (DTC) zones. Interseismic slip rates in the STC zone are estimated using an assumption of creep at constant stress, and interseismic slip rates in the DTC zone are estimated with downdip creep rate gradient profiles consistent with updip propagation of the creeping zone into the locked zone (Bruhat & Segall, 2017). This methodology provides clear delineation of the boundaries of the locked zone, quantification of uncertainties in their location, and insight into how the slip budget is met within the DTC zone.

SHERRILL ET AL. 3 of 21

21699356, 2024, 10, Downloaded from https://agupubs.onlinelibrary.wiley.com/doi/10.1029/2024JB029346 by Indiana University Libraries, Wiley Online Library on [21.03/2025]. See the Terms

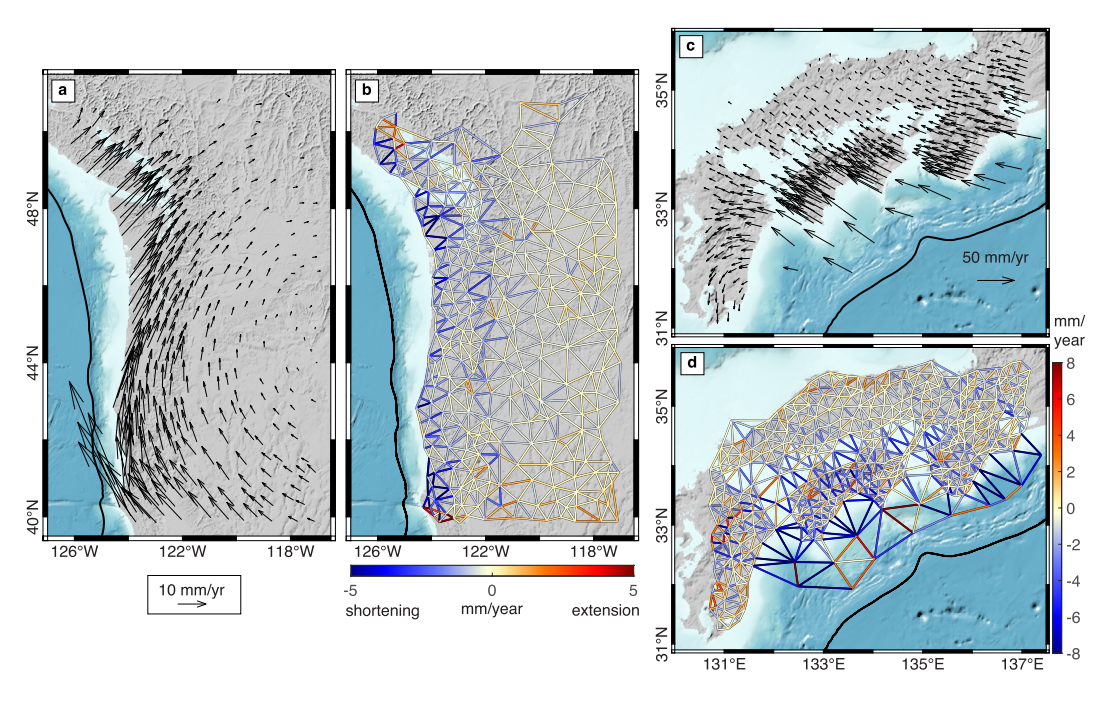


Figure 2. GNSS-derived Interseismic velocities for Cascadia (a) and Nankai (c) in a North America-fixed and Amur-fixed reference frame, respectively. Baseline rate changes for Cascadia (b) and Nankai (d) derived by projecting GNSS-derived velocities into baselines between GNSS stations. Blue (negative difference) indicates shortening and red (positive difference) indicates extension. Dark black line is the trench. We invert baseline rate changes for interface coupling in this study.

2. Data

We utilize previously processed Global Navigation Satellite System (GNSS) geodetic observations of interseismic horizontal velocities for this study. The velocities include contributions from slow slip events as well as more steady deformation since the velocities are averaged over time periods much longer than slow slip events. As described in the following section, we combine and clean the velocity fields and then convert the horizonal velocities to baseline velocity difference rate changes (hereafter referred to as baseline rate changes) and invert the baseline rate changes for our model parameters.

2.1. Cascadia Velocity Data

We use the previously assembled GNSS data for the western United States in a North American reference frame from Zeng (2022). We select stations between $39.8^{\circ}N$ and $51^{\circ}N$ latitude and $-126.5^{\circ}W$ and $-117^{\circ}W$ longitude. To avoid potential local volcanic deformation signals at stations in volcanic areas, we first remove clusters of stations near active volcanoes in California, Oregon, and Washington. Outside of volcanic centers the station distribution is highly irregular in some areas. In areas with numerous closely spaced or repeated station measurements, we discard the station with the highest uncertainty value within a 20 km radius west of the Cascades volcanic arc (around $-121^{\circ}W$) and within a 30 km radius east of the Cascades volcanic arc. After all selections are made, the final dataset has 326 stations (Figure 2a).

2.2. Nankai Velocity Data

We combine two GNSS velocity fields for Nankai (Figure 2c). The first is a set of onshore sites processed by the University of Nevada Reno Geodetic Laboratory using the Median Interannual Difference Adjusted for Skewness (MIDAS) algorithm, which span a time period from 2009 to 2024 (Blewitt et al., 2018), hereafter referred to as the UNR dataset. The second is a set of offshore seafloor sites processed by the Japan Coast Guard (Yokota et al., 2016), hereafter referred to as the JCG dataset. Six stations of the JCG dataset span a time period of 2006–2015, while the other nine stations were installed following the 2011 Tohoku-oki earthquake and span a time period of 2011–2015. We select stations between 31.5°N and 35.5°N latitude and 131°E and 137.5°E longitude. We rotate the UNR dataset to the same fixed Amur plate reference frame as the JCG dataset (DeMets et al., 2010).

SHERRILL ET AL. 4 of 21

21699356, 2024, 10, Downloaded from https://agupubs.onlinelibrary.wiley.com/doi/10.1029/2024JB029346 by Indiana University Libraries, Wiley Online Library on [21.03/2025]. See the Terms

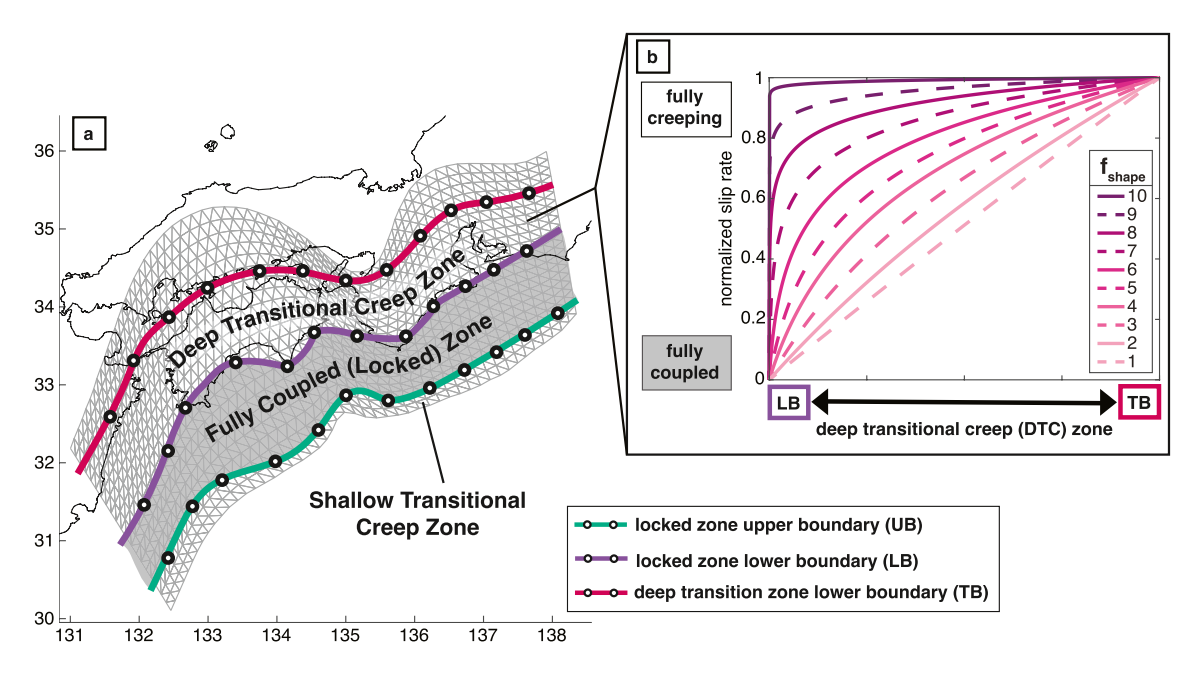


Figure 3. (a) Illustration of the boundaries between the three coupling zones. Gray mesh shows triangular discretization of Nankai subduction interface. The teal line defines the upper boundary at the top the locked zone (LB) and the bottom of the shallow transitional creep zone (STC zone). The purple line defines the boundary at the bottom of the locked zone (LB) and the top of the deep transitional creep (DTC) zone. The dark pink line defines the lower boundary of the DTC zone (TB). Steady creep at the plate rate is assumed below the TB. (b) Parametric representation of creep in the deep transitional creep zone, motivated by the Bruhat and Segall (2017) propagating creep front model. Creep rate divided by plate rate (normalized slip rate) is plotted with normalized distance along the interface in the DTC zone. The different colored curves correspond to varying values of fshape in Equation 1.

First, following methodology of Zeng (2022), we discard stations with differences in azimuthal direction over 20° or amplitudes over 20% from the median of stations within a 5 km radius. Then, in the case of overlapping (or nearby, <5 km apart) stations in the UNR dataset, the station with the greatest uncertainty is discarded. After all selections are made, the final dataset has 426 onshore UNR dataset stations and 13 offshore JCG stations.

2.3. Baseline Rate Changes

We convert the horizontal velocity field for both Nankai and Cascadia to baseline rate changes. First, we construct baselines by using a Delaunay triangulation to connect the GNSS stations (Figures 2b and 2d). Then, we project the GNSS velocity vectors onto unit vectors along baselines. The changes in baseline length capture velocity difference rates between two stations. Rigid body motions produce zero velocity difference rates. Inverting the baseline velocity difference rates for slip on the subduction interface obviates the need to model the entire velocity field using, for example, block models. The baseline method adopted here is similar to the strain rate inversion approach of Johnson et al. (2024). We assume all baseline rate changes are a result of coupling on the interface except at Nankai where we also account for strain across on the Median Tectonic Line by modeling baseline rate changes associated with coupling on the fault, which is estimated in the inversion. We ignore contributions from coupling on crustal faults to baseline rate changes in Cascadia as the slip rates on crustal faults in the region are quite low except near the Mendocino triple junction (Evans et al., 2015; Zeng & Shen, 2017).

3. Boundary Inversion Method

We invert interseismic baseline rate changes for the boundaries of the fully coupled (locked) zone, the deep transitional creep (DTC) zone, and the shallow transitional creep (STC) zone (Figure 3). We use a Bayesian inversion framework and Markov chain Monte Carlo (MCMC) methods to obtain the posterior probability density functions (PDFs) for the zones of interseismic coupling, their boundaries, and the shape of the transition from fully coupled to fully creeping in the DTC zone. We use a forward model for backslip within the inversion. We will first describe this forward model. Then we will explain how it is incorporated in the Bayesian inversion.

SHERRILL ET AL. 5 of 21

3.1. Forward Model

The basis for this model is the same as nearly all subduction zone coupling inversions and utilizes the backslip concept first described by Savage (1983). Under this assumption, all strain in the over-riding plate is attributed to interseismic slip rates on the interface less than the plate rate (slip deficit rate) which is modeled with backwards slip (i.e., opposite to relative plate motion) using the solution for dislocations in a homogeneous elastic half-space. In the forward model, the subduction interface is discretized into triangular elements of nominal side length of 15 km and the interface is divided into three zones with three boundaries as illustrated in Figure 3a. The locked zone is defined as the area between the upper (UB; teal line in Figure 3a) and lower (LB; purple line in Figure 3a) locked zone boundaries and is fully coupled (zero creep rate). The STC zone is defined as the area between the trench and the UB and is partly coupled with creep rate in this zone occurring at constant stress (equivalently, zero stressing rate). The DTC zone is defined as the area between the LB and the transition zone boundary (TB; pink line in Figure 3a) and is partly coupled with an imposed functional form for creep with depth. We define each of the three boundaries (UB, LB, and TB) as a set of nodes connected by a spline function. We fix position of the nodes along strike and solve for their depth.

3.1.1. Locked Zone Backslip Rate

For elements within the locked zone (between UB and LB), we impose backslip at the plate rate in the direction of relative plate motion to cancel all of the forward slip on the interface (fully coupled).

3.1.2. Deep Transitional Creep Zone Backslip Rate

We assume the subduction interface transitions from fully coupled at LB to fully creeping at TB, and accordingly the entire DTC zone is partly coupled. Motivated by Bruhat and Segall (2017), we approximate the depth-dependent creep rate distribution in the DTC zone due to updip propagation of the lower creep front using a logarithmic function of the form

$$\dot{s}(z) = \frac{v_{pl}}{log(1 + 2a/f_{hape})} log\left(1 + \frac{a - z}{f_{hape}}\right),\tag{1}$$

where v_{pl} is the plate convergence rate, a is the half width of the DTC zone, z is the distance along the interface from the center of the DTC zone, and f_{shape} is a shape factor that determines the steepness of slip rate gradient (Figure 3b). We select this logarithmic function because it approximates the steep creep rate distribution of Bruhat and Segall (2017) while requiring only one shape parameter. The parameter f_{shape} is assigned at the same nodes used to define the boundaries. The shape of creep rate distributions with normalized distance from the center of the transition zone is illustrated in Figure 3b for a range of f_{shape} values. To make sampling of f_{shape} more efficient, we use discretized steps and only allow one of the 10 slip rate profile shapes shown in Figure 3b to be selected. We number the f_{shape} values from 1 to 10 with one being the least steep and 10 being the most steep. The actual values corresponding to the ten f_{shape} values are provided in Supplementary Table S1 in Supporting Information S1.

3.1.3. Shallow Transitional Creep Zone Backslip Rate

Imposing a functional form on creep rates in the STC zone is not as straightforward as for the DTC zone because the creep rate at the trench is unknown and we cannot assume it is fully creeping as we do at the bottom of the transition zone (TB). Instead, we use a boundary element calculation to compute the creep rate in the STC zone. Similar to previous methods (Herman et al., 2018; Johnson, 2013; Lindsey et al., 2021), we assume that interseismic creep occurs steadily at zero stressing rate. Therefore, any backslip in the STC zone is releasing shear stress imposed by backslip on all patches of the subduction interface. We compute the vector of shear stressing rates at the center of fault patches in the STC zone, $\dot{\tau}_{stc}$, due to the vector of backslip rates on fault patches outside the STC zone, \dot{s}_{out} , using the relation of

$$\dot{\tau}_{stc} = G_{out} \dot{s}_{out} \tag{2}$$

SHERRILL ET AL. 6 of 21

where G_{out} is a matrix of stress Green's functions that relate stressing rates on patches in the STC zone due to backslip outside the STC zone and is constructed using the Okada (1992) dislocation solution. We require the stressing rate inside the STC zone to be zero,

$$G_{in}\dot{s}_{in} + \dot{\tau}_{stc} = 0 \tag{3}$$

where \dot{s}_{in} are slip rates on patches in the STC zone and G_{in} is a matrix of corresponding stress Greens functions. We then compute backslip rates on the fault patches in the STC zone, \dot{s}_{in} ,

$$\dot{s}_{in} = -(G_{in})^{-1} \, \dot{\tau}_{stc}. \tag{4}$$

3.2. Inversion in Bayesian Framework

Several parameters that are nonlinearly related to the data are required to compute backslip in the forward model described in the previous section: first, vectors of the depths of nodes defining the three boundaries; z_{UB} , z_{LB} , and z_{TB} ; second, a vector of DTC shape factors for each along strike node location, f_{shape} ; third, a scalar convergence rate factor, f_{CR} , used to scale v_{pl} to account for uncertainties in v_{pl} and the fact that not all of the plate convergence is accommodated by the subduction interface; and lastly, an optional vector of backslip rates on model continental crustal faults crossing baselines, \dot{s}_{cf} . For notational purposes, we combine these unknown parameters into a vector of unknowns, $m = \begin{bmatrix} z_{UB}^T, z_{LB}^T, z_{TB}^T, f_{shape}^T, f_{CR}, \dot{s}_{cf}^T \end{bmatrix}$. Invoking Bayes' Theorem, we seek the posterior PDF of the unknown model parameters given a vector of observed baseline rate changes, d,

$$p(m|d) \propto p(d|m) p(m),$$
 (5)

where p(d|m) is the likelihood and p(m) is the prior PDF of the nonlinear model parameters. The likelihood is constructed assuming Gaussian data errors and covariance matrix, Σ ,

$$p(d|m) \propto exp\left[-\frac{1}{2}(d - G(m))^T \Sigma^{-1}(d - G(m))\right],\tag{6}$$

where G(m) is the nonlinear relationship between model parameters and predicted surface deformation. For this study, we neglect data covariances and assume a diagonal covariance matrix. There is no prior covariance between the parameters (i.e., nodes, f_{shape}).

The priors distributions for all nonlinear model parameters, p(m), are uniform with bounds implemented for z_{UB} , z_{LB} , z_{TB} , and f_{CR} . The bounds set on the node depths are $z_{trench} > z_{UB} > z_{LB} > z_{TB} > z_{slab_bot}$, where z_{trench} is the depth of the trench and z_{slab_bot} is the depth of the bottom of the slab model (80–100 km). The bounds on f_{CR} allow for an increase or decrease of v_{pl} by up to 15%. We estimate two different values for f_{CR} at Cascadia: one for the subducting Gorda plate and one for the rest of the subducting slab (Chaytor et al., 2004). The prior for f_{shape} is a discrete uniform distribution of integers ranging from 1 to 10.

We construct the posterior PDF of nonlinear parameters, p(m|d), using the Markov chain Monte Carlo (MCMC)-Metropolis sampling algorithm (e.g., Fukuda & Johnson, 2010; Gamerman, 1997; Gilks & Roberts, 1996; MacKay, 2003; Metropolis et al., 1953). Specific details about the MCMC setup, priors, and posterior PDFs are provided in Table S2 and Figures S1–S5 in Supporting Information S1.

4. Boundary Inversion Results

We present the boundary inversion results for both Nankai and Cascadia in this section. First, we present the probability distributions of the upper boundary of the locked zone (UB), the lower boundary of the locked zone (LB), and the lower boundary of the deep transitional creep (DTC) zone (TB) and the probability distribution of the locked zone. Then, we present the fit of the model to the baseline rate change data. Lastly, we present slip rate profiles for interseismic slip from the trench to the bottom of the DTC zone at various profiles along strike.

We will discuss the prominent features for northern Cascadia (north of 46°N), central Cascadia (42.5–46°N), and southern Cascadia (south of 42.5°N) following a similar segmentation discussed in Bartlow (2020). We will

SHERRILL ET AL. 7 of 21

21699356, 2024, 10, Downloaded from https://agupubs.onlinelibrary.wiley.com/doi/10.1029/2024/B029346 by Indiana University Libraries, Wiley Online Library on [21.032025]. See the Terms and Conditions (https://onlin

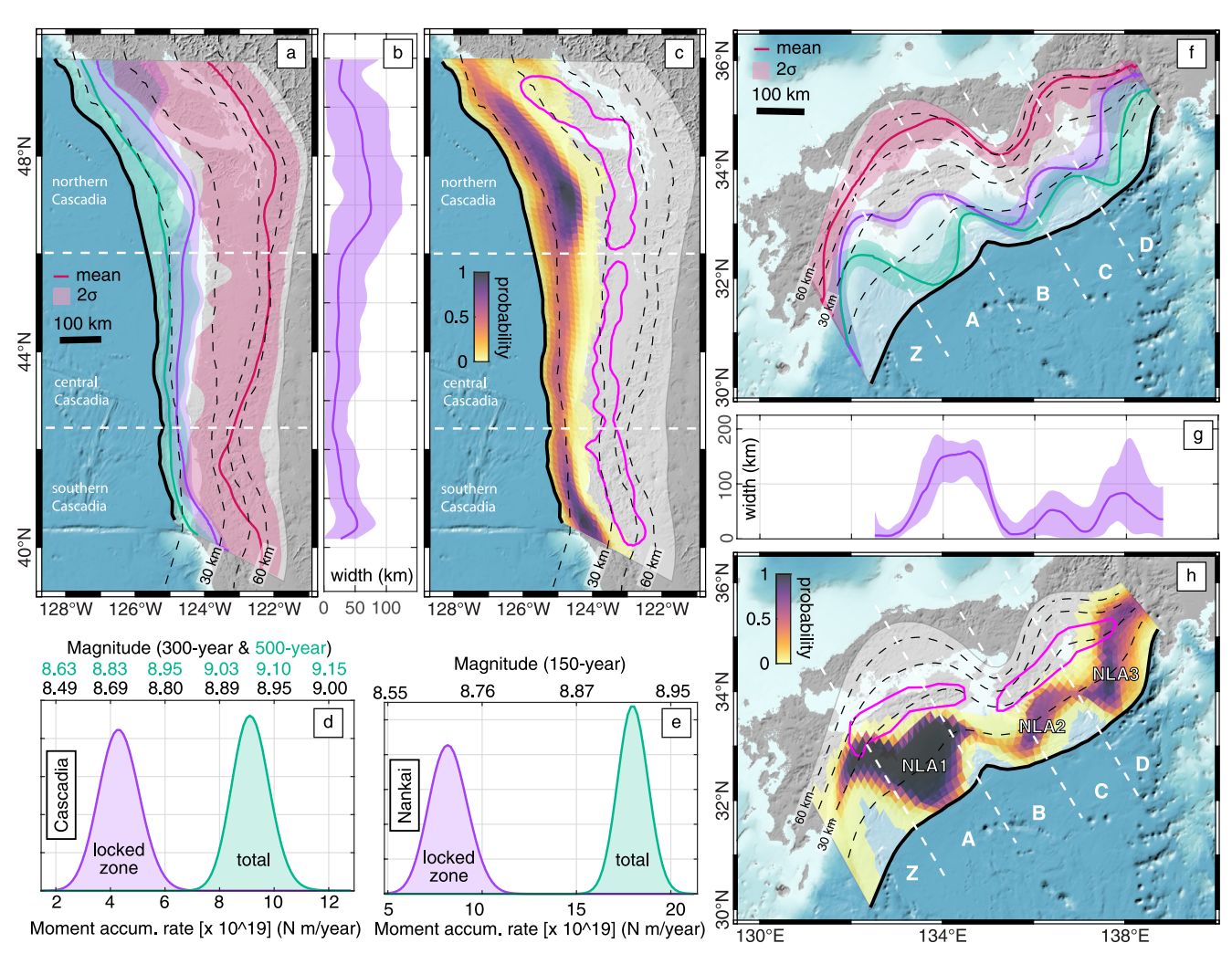


Figure 4. Summary of estimated boundary locations, locked zone, and moment accumulation rates. Median (solid line) and 2σ (shaded polygon) locations of UB (teal), LB (purple), and TB (pink) at Cascadia (a) and Nankai (f). Along-dip width of the locked zone at Cascadia (b) and Nankai (g). Locking probability distributions at Cascadia (c) and Nankai (h). Color shows the probability that a patch on the interface is in the locked zone. Pink outlines represent the boundaries of the ETS zone. The three locked areas of Nankai are labeled as NLA1, NLA2, NLA3. Probability distributions of moment accumulation rate at Cascadia (d) and Nankai (e) within the locked zone (purple) and over the entire interface (total; teal color). Equivalent moment magnitude is shown assuming steady moment accumulation rate over 300 or 500 years for Cascadia and 150 years for Nankai. Black dashed contour lines represent slab depth at Nankai and Cascadia in 15 km increments (Hayes et al., 2018; Nakanishi et al., 2018). White dashed lines show the regional boundaries for both subduction zones.

discuss prominent features at Nankai for five regions (moving from west to east); the Hyuganada region (Z; east of 132.3°E), the Nankai-Shikoku region (A; 132.3–134.3°E), the Nankai-Kii Channel region (B; 134.3–135.9°E), the Tonankai-Kii Peninsula region (C; 135.9–136.9°E), and the Tonankai-Ise Bay region (D; 136.9–138.2°E). We use the letter naming convention of Hirose et al. (2022) for the Nankai regions.

4.1. Boundary Locations

Figure 4a shows the median (solid line) and 2σ (shaded polygon) locations of UB (teal), LB (purple), and TB (pink) at Cascadia. Table 1 provides the average depth and standard deviations for each of the three regions in Cascadia. LB is trenchward of the coastline nearly everywhere and, within 2σ uncertainty, is constrained to 13–27 km depth in northern Cascadia, 7–21 km depth in central Cascadia, and 9–17 km in southern Cascadia. The median depth of UB is ~8–10 km depth across all three Cascadia regions, indicating potential shallow creep in these regions. However, within 2σ uncertainty, the depth of UB may be located anywhere between the depth of the trench and 23 km in northern Cascadia, 19 km in central Cascadia, and 14 km in southern Cascadia. We find that TB is deepest in the central Cascadia region (65 km) and shallowest in southern Cascadia (51 km). There is

SHERRILL ET AL. 8 of 21

21699356, 2024, 10, Downloaded from https://agupubs

	Up	Upper boundary (UB)			Lower boundary (LB)			Transition boundary (TB)		
	-2σ	Median	+2\sigma	-2σ	Median	$+2\sigma$	-2σ	Median	$+2\sigma$	
North	3.78	10.35	22.61	13.05	19.41	26.96	24.76	59.03	96.95	
Central	3.76	8.65	18.67	6.72	14.03	20.73	25.53	64.70	98.69	
South	3.76	7.91	13.86	8.67	13.35	17.27	19.43	50.66	95.65	

considerable uncertainty on the location of TB at Cascadia (up to \sim 75 km depth variation). This is likely due to a combination of high data uncertainty relative to observed velocities above the transition zone, a steeper dip in the slab further inland, and a tradeoff between the location of TB and the shape of the DTC zone slip distribution. While the location of UB appears quite uncertain, the confidence intervals illustrated in Figure 4a do illustrate that the UB depth and LB depth tend to correlate positively such that deeper UB depths correlate with deeper LB depths. Figure 4d shows the posterior probability density of total moment accumulation rate within the locked zone is 4.35×10^{19} N m/year ($\pm 1.40 \times 10^{19}$ N m/year; purple distribution on Figure 4d) and that the moment accumulation rate across the entire interface is 9.13×10^{19} N m/year ($\pm 1.29 \times 10^{19}$ N m/year; teal distribution on Figure 4d). Thus, the moment accumulation rate in the locked zone is approximately 48% of the total moment accumulation rate on the entire interface.

Figure 4f shows the median (solid line) and 2σ (shaded polygon) locations of UB (teal), LB (purple), and TB (pink) at Nankai. Table 2 provides the average depth and standard deviations for each region in Nankai. In regions A and D, the median depth of UB is \sim 8–12 km depth, but within 2σ uncertainty may extend to the trench or as deep as 23 km. In region Z, the depth of UB, with 2σ uncertainty, is well below the depth of the trench. LB tends to follow the coastline in regions A and C and extends to 14–25 km depth. Notably, in regions Z, B, and near the transition from region C to region D, UB and LB are very near each other indicating little to no locked zone in these regions. TB varies from a minimum depth of 50 km in region A to maximum depth of 58 km in region B. Even within 2σ uncertainties there are discernible STC zones, locked zones, and DTC zones all along strike at Nankai. Figure 4e shows the posterior probability densities of moment accumulation rate in the locked zone and across the entire interface at Nankai. We estimate the mean moment accumulation rate in the locked zone at Nankai to be 8.27×10^{19} N m/year ($\pm 1.89 \times 10^{19}$ N m/year; purple distribution on Figure 4e) and the moment accumulation rate across the entire interface to be 17.95×10^{19} N m/year ($\pm 1.45 \times 10^{19}$ N m/year; teal distribution on Figure 4e). Therefore, the moment accumulation rate in the locked zone is approximately 46% of the total moment accumulation rate at Nankai.

4.2. Locked Zone Probability Distributions

Each realization in the Markov chain contains a map of binary locking parameters with locked patches having a value of one and creeping patches having a value of zero. The posterior distribution of the binary locking parameter is the collection of these ones and zeros. Figures 4c and 4h show the mean of all realizations for each patch, that is the probability of locking, at Cascadia and Nankai. Patches that were locked in every realization return a probability value of one, whereas patches that are not locked in every realization return a probability value

 Table 2

 Regional Median Depths and Standard Deviations for Nankai Boundaries

	Upper boundary (UB)			Lower boundary (LB)			Transition boundary (TB)		
	-2σ	Median	$+2\sigma$	-2σ	Median	+2\sigma	-2σ	Median	+2\sigma
Z	18.36	25.12	33.73	28.43	34.83	42.27	38.06	53.43	68.69
A	5.17	7.92	12.83	22.35	24.63	26.73	38.31	50.18	65.90
В	8.06	10.57	14.23	10.42	13.65	17.46	44.67	57.96	69.50
C	9.43	12.09	16.98	11.11	19.09	23.76	37.19	54.97	69.40
D	5.27	12.54	23.02	15.47	25.66	36.05	37.87	56.54	69.72

of zero. The high probability areas in Figures 4c and 4h correspond to the area between the teal and purple boundaries on Figures 4a and 4f. Figures 4b and 4g show the mean (solid line) and 2σ (shaded polygon) of the width of the locked zone along strike at Cascadia and Nankai.

At Cascadia, we find the locked zone is widest and deepest, on average, in the northern region (Figure 4b), similar to prior studies (e.g., Li et al., 2018; Lindsey et al., 2021; Pollitz & Evans, 2017; Schmalzle et al., 2014). We estimate that the locked zone in northern Cascadia has a mean width of 22–75 km and extends as deep as 21.62 km (near 47°N). We infer a very narrow locked zone in central Cascadia (mean width of 13–26 km and, on average, extending to a maximum depth of 15.67 km). Within 2σ uncertainty, the width of the locked zone in central Cascadia may be as narrow as 0 km or as wide as

SHERRILL ET AL. 9 of 21



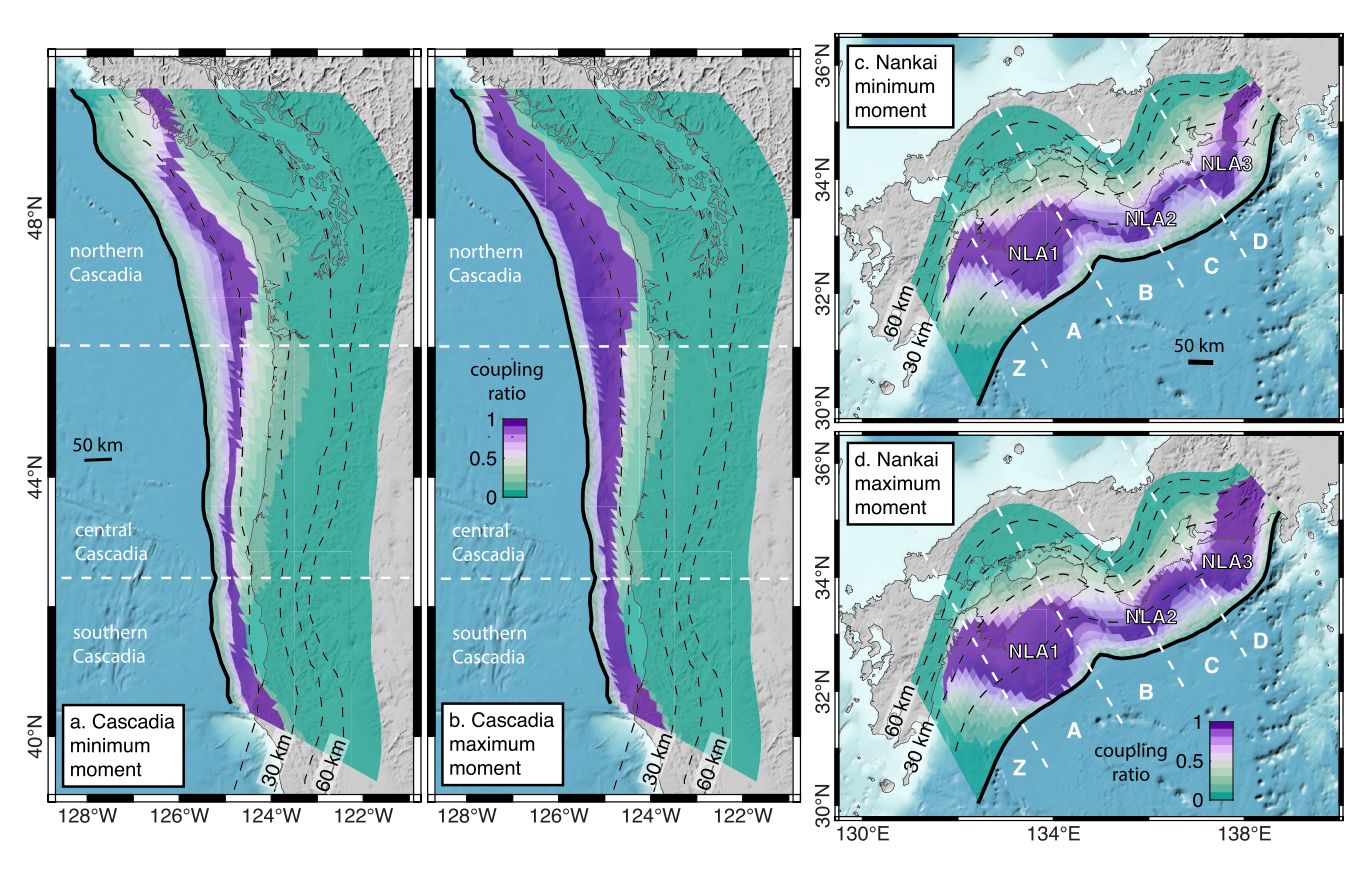


Figure 5. Coupling ratio for the minimum (a) and maximum (b) locked zone moment accumulation rates at Cascadia and for the minimum (c) and maximum (d) locked zone moment accumulation rates at Nankai. The three locked areas of Nankai are labeled as NLA1, NLA2, and NLA3. Black dashed contour lines represent slab depth at Nankai and Cascadia in 15 km increments (Hayes et al., 2018; Nakanishi et al., 2018). White dashed lines show the regional boundaries for both subduction zones.

34 km, indicating we cannot rule out a fully creeping central region nor can we rule out a fully coupled central region. In southern Cascadia, locking extends to a maximum depth of 33.88 km, but more careful modeling needs to be done to account for complex tectonics at the Mendocino triple junction.

We identify three persistent locked areas at Nankai. The first Nankai locked area (NLA1) is located mostly in region A (offshore of Shikoku and centered on 133.5°E, 33.6°N) and is roughly 200 km along strike and 150 km along dip. The second Nankai locked area (NLA2) is located in the western half of region C (southeast of Kii peninsula and centered on 136°E, 33°N) and is roughly 95 km along strike and 60 km along dip. The third Nankai locked area (NLA3) is located in region D (offshore of Shima Peninsula, near Ise Bay, and centered on 137.5°E, 34°N) and is roughly 180 km along strike and 95 km along dip. We estimate no locked zone at all in region B and a very limited (<30% probability) locked zone between regions C and D.

While there is considerable uncertainty in the location of the locked zone boundaries and the width of the locked zones, especially for Cascadia, the plots in Figure 4 do not capture the correlations in boundary locations, f_{shape} , and f_{CR} . Figure 5 shows the coupling ratio models associated with the bottom 5% and top 5% moment accumulation rates in the locked zones at Cascadia and Nankai, named hereafter minimum and maximum moment accumulation rate models. They are computed using the forward model (Section 3.1) with the mean nonlinear model parameters of the realizations within the bottom 5% and top 5% moment accumulation rates. Specific examples of the correlations between the inversion parameters are provided for select profiles in Supplementary Figures S6 and S7 in Supporting Information S1. At Cascadia the maximum moment accumulation rate model displays a locked zone from ~8 to 20 km depth in the north and ~8–10 km depth in the south. The minimum moment accumulation rate model in Cascadia displays a narrower locked zone along the entire margin, but nowhere is there a fully creeping segment without locking. The uncertainty on the size of the locked zones at Nankai is considerably smaller than at Cascadia. NLA1 is nearly identical in the minimum and maximum moment maps for Nankai. However, the size and location of NLA2 and the size of NLA3 have more variance due to

SHERRILL ET AL. 10 of 21

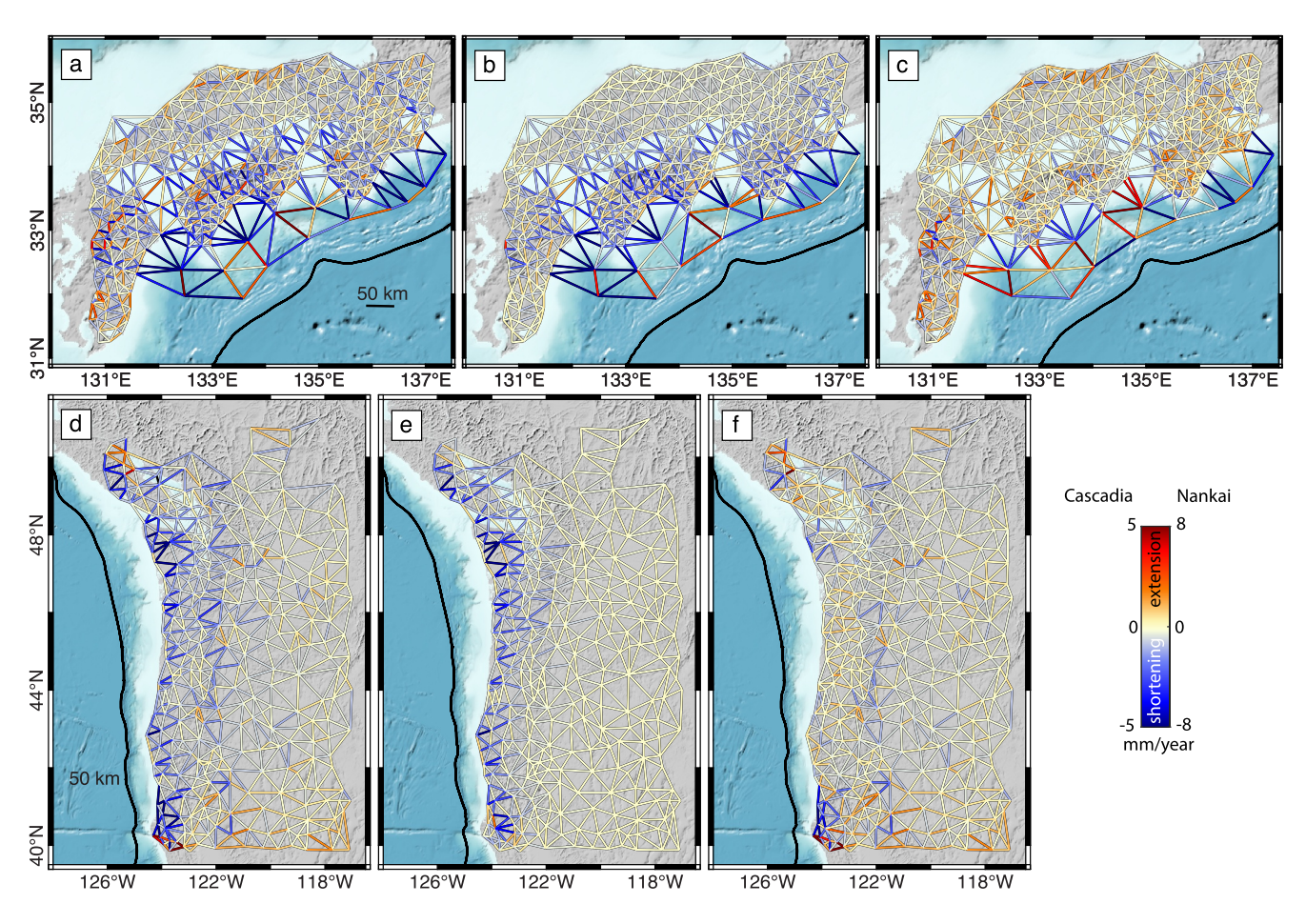


Figure 6. Observed (a), modeled (b), and residual (c) baseline rate changes for Nankai. Observed (d), modeled (e), and residual (f) baseline rate changes for Cascadia. Blue indicates shortening (negative rate) and red indicates extension (positive rate).

greater uncertainties in a few of the offshore sites in this region. The posterior distribution of NLA2 alternates between a deeper, broader locked patch reaching near the coast of Kii peninsula and shallower locked patch at the trench extending to \sim 50 km seaward of the coast of Kii peninsula.

4.3. Model Fit

Figure 6 illustrates the fit to the data utilizing the mean modeled baseline rate changes for Cascadia and Nankai. The color of the lines represents their magnitude, where red indicates extension and blue indicates shortening. Key patterns in the observed baseline rate changes at Cascadia are high shortening rates along the coast with the highest rates in northern and southern Cascadia, a decay in shortening rates to the east, and a mix of high shortening rates and high extension rates near 40°N. While the velocity data were cleaned thoroughly before modeling, there are still some outliers (near -122°E , 44°N ; -121.5°E , 41.5°N ; and -121°E , 47°N) that are highlighted due to the nature of converting velocities to baseline rate changes. These high strain rates may be due to viscoelastic effects not fully modeled by an elastic earth model or strain from unmodeled crustal faults. We are able to match the high shortening rates along the coast with high values in the north and south as well as the eastward decay in shortening rates. However, we do not get as much shortening in our model as is observed east of

 -121° E. We estimate our model's ability to explain the data using variance reduction, $VR = 1 - \frac{\sum (d-\hat{d})^2}{\sum d^2}$, where

d is the data vector and \hat{d} is the model output vector. We compute a variance reduction of 59% for the mean model fit of the baseline rate changes to observed. Some of the misfit may be due to the inability to model the complicated tectonics of the Mendocino triple junction with our model, as mentioned previously.

SHERRILL ET AL. 11 of 21

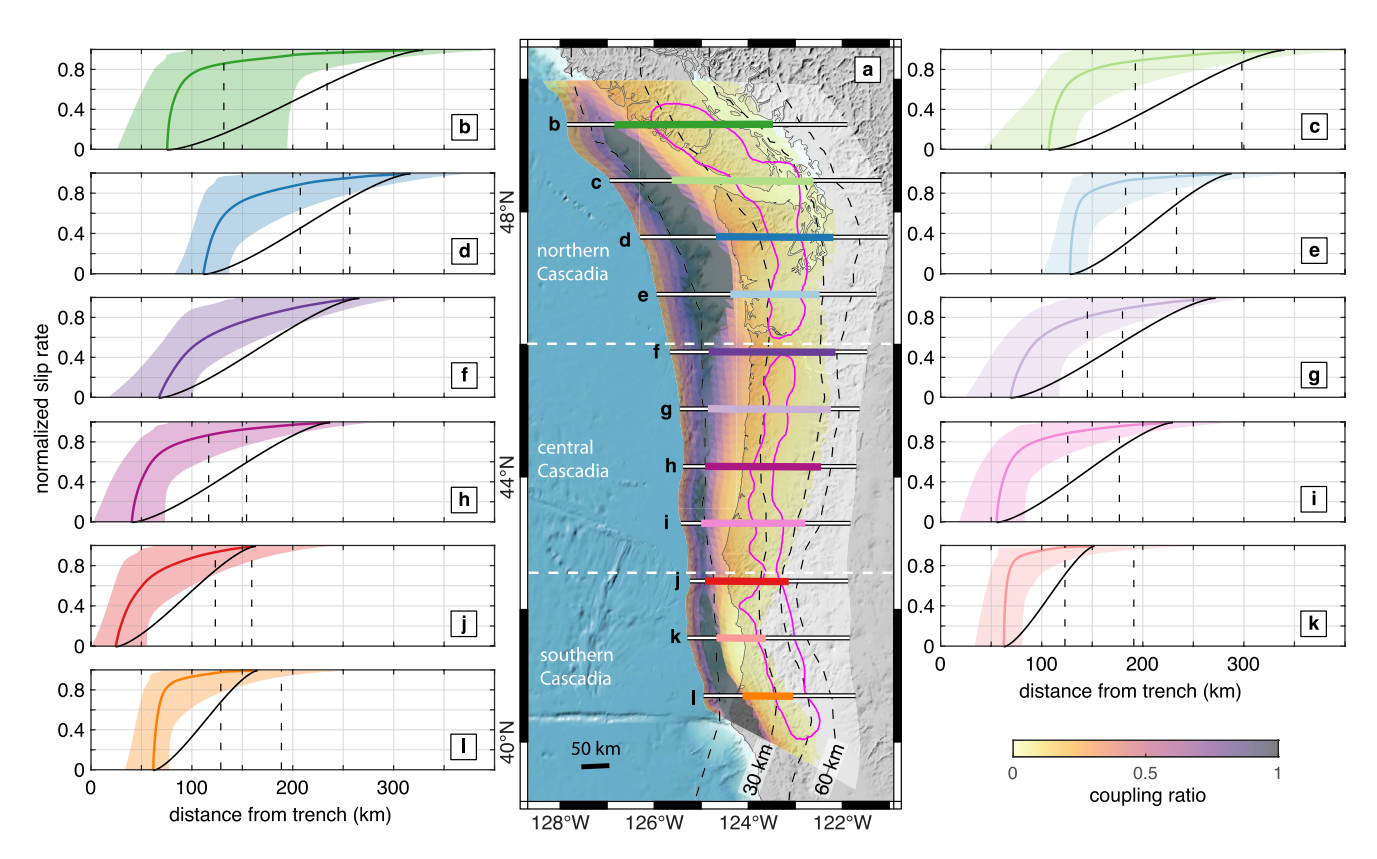


Figure 7. Illustration of creep rate with depth within the deep transitional creep zone (DTC) at Cascadia. (a) Median coupling ratio in map view at Cascadia. Pink polygons represent the approximate location of the ETS zone at Cascadia. (b–l) Posterior distribution of interseismic creep rate profiles for cross-sections b-l showing the median (solid line) and 2σ (shaded polygon) locations of the distributions. The slip rates are normalized by the convergence rate so they range from 0 (locked) to 1 (fully creeping). This is opposite to the coupling ratio. The solid black lines show the computed transition zone shape for the DTC zone under the assumption of no creep front propagation (stationary locking) and creep at constant stress. Dashed black lines show the locations of the top and bottom edges of ETS zone within each profile. Black dashed contour lines on (a) represent slab depth at Cascadia in 15 km increments (Hayes et al., 2018). White dashed lines on (a) show the regional boundaries for Cascadia.

Key patterns in the observed baseline rate changes at Nankai are high shortening rates along the southern coast; a decay of shortening rates toward the Sea of Japan; a faster decay of shortening rates across Shikoku and western Honshu (regions A and B) than in regions Z, C and D; and lower shortening rates offshore than onshore. We are able to match the high shortening rates along the coast, the faster shortening decay rate in regions A and B, and the lower shortening rates offshore. We are unable to match the magnitude of shortening and extension across Kyushu (in region Z) nor the shortening rates along the northern coast of Honshu. We suspect there are non-subduction related deformation sources causing these patterns. We estimate a variance reduction of 68% for the mean model fit of the observed baseline rate changes at Nankai.

4.4. Interseismic Slip Rate Profiles

Figures 7 and 8 show the median coupling ratio in map view (middle) and the median (solid line) and 2σ (shaded polygon) interseismic slip rates for cross-sections across the subduction interface (surrounding figures) for Cascadia and Nankai, respectively. We provide the expected transition zone shape for the DTC zone (black lines on surrounding figures) for the assumption of creep at constant stress (stationary locked zone) for reference. Dashed lines on the surrounding figures show the approximate range of the distance from the trench where episodic short-term slow slip events are observed.

Our results indicate a tendency for the transition from fully coupled to fully creeping to be moderately steep to very steep (all f_{shape} values ranging from 5 to 9; Figures 7b–7l) at Cascadia. The inversion prefers a steep distribution ($f_{shape} = 8$) in northern and southern Cascadia and a moderately steep distribution ($f_{shape} = 6$) in central Cascadia (Figures 7b–7l). The least steep distribution, with an f_{shape} value of 5, occurs at the northern to central

SHERRILL ET AL. 12 of 21

21699356, 2024, 10, Downloaded from https://agupubs.onlinelibrary.wiley.com/doi/10.1029/2024/B029346 by Indiana University Libraries, Wiley Online Library on [21/03/2025]. See the Terms

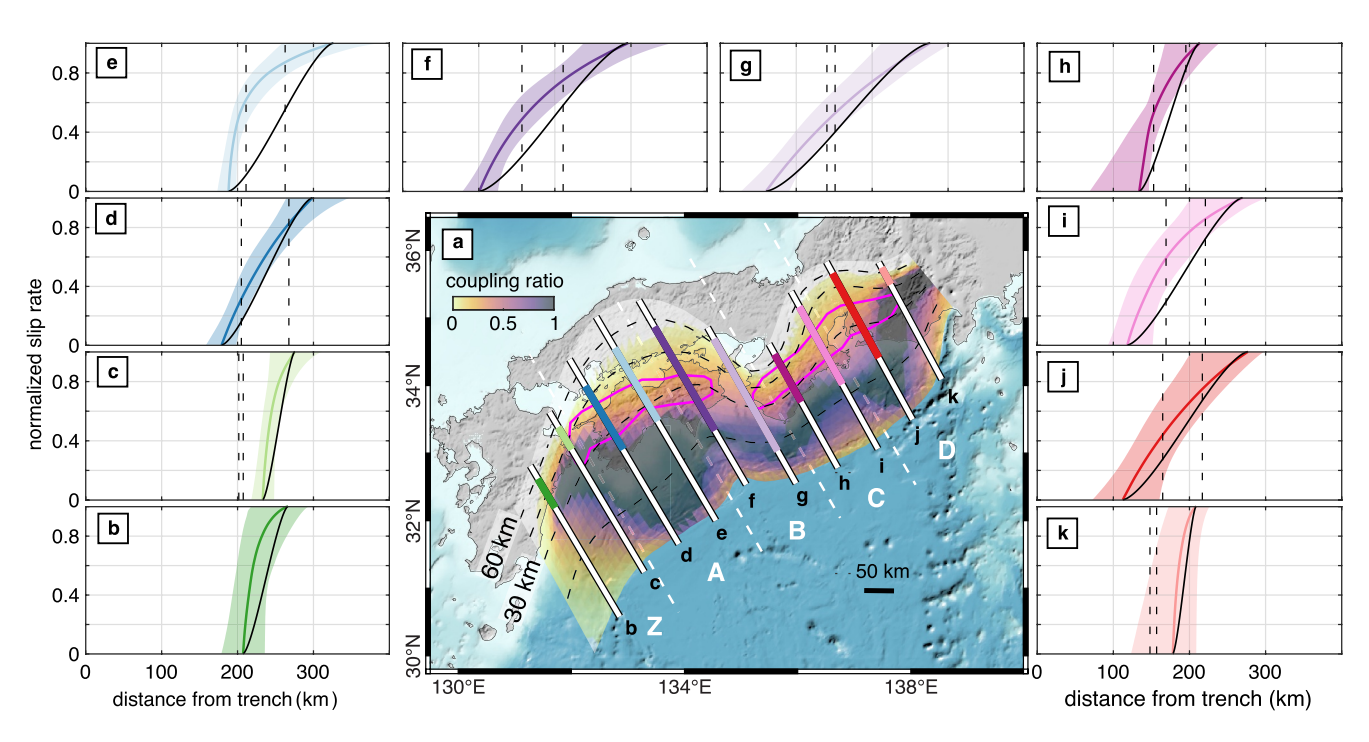


Figure 8. Same as Figure 6 for Nankai. (a) Median coupling ratio in map view at Nankai. Pink polygons represent the approximate location of the ETS zone. (b)–(k) Posterior distribution of interseismic creep rate profiles for cross-sections b-l showing the median (solid line) and 2σ (shaded polygon) locations of the distributions. The slip rates are normalized by the convergence rate so they range from 0 (locked) to 1 (fully creeping). This is opposite to the coupling ratio. The solid black lines show the computed transition zone shape for the DTC zone under the assumption of no creep front propagation (stationary locking) and creep at constant stress. Dashed black lines show the locations of the top and bottom edges of ETS zone within each profile. Black dashed contour lines represent slab depth at Nankai in 15 km increments (Nakanishi et al., 2018). White dashed lines show the regional boundaries for Nankai.

Cascadia boundary (\sim 46°N, Figure 7f). To examine why the baseline rate data favor steep creep rate gradients at Cascadia, we also conducted an inversion with the shape factor fixed to the linear end-member ($f_{shape} = 1$). Figure S7 in Supporting Information S1 shows that this inversion systematically misfits baseline rates because it does not produce enough shortening near the coastline (especially around -124° W, 47.5° N) and it produces too much shortening directly inland of that area and in a narrow band extending down to 42° N. We infer a gap between the top of the ETS zone and the bottom of the locked zone inferred along strike and ranging from 25 to 90 km in map view. The median distributions (solid lines in Figures 7b–7k) suggest there may be a slip deficit of 0%–20% in the ETS zone and that S-SSEs in the ETS zone are not completely filling the slip budget. Within 95% confidence this may increase to as high as 40% slip deficit.

Our results indicate a tendency for the transition from fully coupled to fully creeping to be straight to moderately steep (all f_{shape} values ranging from 2 to 6; Figures 8b–8k) at Nankai. In region Z (furthest west), the DTC zone is very narrow (25–50 km in map view) and the shape of the distribution is slightly steep ($f_{shape} = 4$ –5, Figures 8b and 8c). In region A (Nankai-Shikoku), the distributions transition from straighter ($f_{shape} = 2$, Figure 8d) to being moderately steep ($f_{shape} = 6$, Figure 8e). Cross section e has the highest shape factor of all and is the steepest at Nankai. In region B (Nankai-Kii channel), the distributions transition from slightly steep ($f_{shape} = 3$, Figure 8f) back to being straighter ($f_{shape} = 2$, Figure 8g). The region C (Kii Peninsula) transition zone shape has the most variance in f_{shape} and the location of the LB and UB boundaries (Figure 8h). This is where the posterior distribution of NLA2 alternates between deeper locking near the coastline and shallower locking near the trench (illustrated by the uncertainty of where the slip rate distribution crosses the x-axis in Figure 8h and in the LB PDF Figure S3h in Supporting Information S1). The transition zone distributions alternate from steep to straight, respectively. The median shape factor for region C is 2 and, within 2σ uncertainty, straighter distributions are likely. Moving from region C to region D (Kii-Ise Bay), the transition zone is moderately steep again ($f_{shape} = 4$, Figure 8i) then returns to relatively straight ($f_{shape} = 2$, Figures 8j and 8k). Unlike Cascadia, there is little to no gap between the ETS zone and LB (a maximum of 50 km in map view). The top of the ETS zone is especially close to LB at cross sections d and h. The median distributions suggest there may be a slip deficit of 25%-60% in the ETS

SHERRILL ET AL. 13 of 21

zone and that S-SSEs in the ETS zone are not completely filling the slip budget. Within 95% confidence this may increase to as high as 70% slip deficit.

5. Discussion

5.1. Comparison to Estimates of Past Earthquakes and Coupling - Cascadia

In summary, moment accumulation in the locked zone, at the present-day moment accumulation rate over a 300–500 years earthquake cycle, is comparable to the lower end of magnitude estimates for the 1700 earthquake and the largest differences between the maximum and minimum moment coupling maps are largely in the shallow depths near the trench where there is a lack of data. Figure 4d shows the probability distributions of moment accumulation rate within the locked zone and across the entire interface for Cascadia. Based on the moment accumulation rates computed in Section 4.1, we estimate that the locked zone alone is capable of hosting an earthquake with a moment magnitude of $M_{\rm w}$ 8.71 \pm 0.09 for a 300-year earthquake cycle and a moment magnitude of $M_{\rm w}$ 8.85 \pm 0.09 for a 500-year earthquake cycle (purple distribution in Figure 4d). The 1700 Cascadia earthquake has been estimated from Japanese tsunami records as M8.7-M9.2 (Satake et al., 2003). Even at our upper bound of magnitude, there is not enough moment accumulation at the current rate in the current locked zone alone to reach a M9.2 event. We estimate that a total release of moment accumulation on the entire interface at the current rate could result in a 300-year $M_{\rm w}$ of 8.92 \pm 0.04 and a 500-year $M_{\rm w}$ of 9.07 \pm 0.04 (teal distribution in Figure 4d). Thus, the high end of magnitude estimates would require significant moment release from outside the locked zone. It is also possible that some moment is released postseismically, as is discussed in the following section for Nankai.

Figures 5a and 5b show the coupling ratio for the minimum and maximum locked zone moment accumulation rates for Cascadia. Key differences between the two maps are the presence of shallow creep in northern Cascadia, a thinner locked zone width along the entire margin, and a broader transition zone in central Cascadia in the minimum moment map (Figure 5a). Currently ongoing seafloor geodesy experiments should result in offshore velocity data in Cascadia within the next few years, which should provide better constraints on the offshore coupling state. The highly coupled regions in our coupling maps are in agreement with the broad features of most coupling maps for Cascadia (e.g., Li et al., 2018; Lindsey et al., 2021; Pollitz & Evans, 2017; Schmalzle et al., 2014) including the deepest and widest locked region in northern Cascadia and the narrowest and shallowest locked region in central Cascadia. Schmalzle et al. (2014) assert that central Cascadia is creeping and cite evidence of reduced interseismic uplift rates, coseismic subsidence, and ETS activity relative to northern and southern Cascadia to support this assertion. Ramos et al. (2021) show that the amount of slip deficit in the central Cascadia region may be a major controlling factor on the eventual size of a Cascadia megathrust earthquake. We find that the locked zone is indeed narrower and shallower in central Cascadia, but the inversion results suggest the existence of a locked zone even for the minimum moment rate model. We cannot rule out the possibility of a fully creeping central region given the large uncertainties on the boundary locations (Figure 4a), but it is evident that this central section does not need to be creeping at all depths to explain the data. Similar to Schmalzle et al. (2014), we find that the transition zone in central Cascadia is broader with lower creep rate gradients than in northern or southern Cascadia.

5.2. Comparison to Estimates of Past Earthquakes and Coupling - Nankai

We assert that the current moment accumulation rate in the locked zone results in magnitude estimates greater than most estimates of past Nankai earthquakes and there is even less variation between the minimum and maximum moment coupling maps, relative to Cascadia, due to better constraints in the offshore region. Figure 4e shows the probability distributions of moment accumulation rate within the locked zone and across the entire interface for Nankai. Given the moment accumulation rate computed in Section 4.1, we estimate that the locked zone is capable of hosting an earthquake with a moment magnitude of M_w 8.70 \pm 0.06 earthquake, assuming a 150-year earthquake cycle (purple distribution in Figure 4e). Most of the uncertainty is in the offshore region where the fit to data is poorer (Figure 6f). We estimate that a total release of moment accumulation for 150 years on the entire interface could result in an earthquake with a moment magnitude of M_w 8.92 \pm 0.03 (teal distribution in Figure 4e). The 1707 Hoei earthquake, which is thought to have ruptured nearly the entire interface has an estimated M_w of 8.4–8.7 (Annaka, 2003; Chesley et al., 2012; Furumura et al., 2011). Some of the moment accumulation in the unlocked portions of the interface may also be relieved in afterslip immediately following an

SHERRILL ET AL. 14 of 21

21699356, 2024, 10, Downloaded from https://agupubs

Table 3

Moment Accumulation Rate and Magnitude of Each Nankai Region

	Locked zone		Full interface		
Region	Moment accumulation rate (N m/yr)	$M_{\rm w}$	Moment accumulation rate (N m/yr)	$M_{ m w}$	
Z	1.16×10^{19}	8.12	2.83×10^{19}	8.38	
A	3.84×10^{19}	8.47	5.37×10^{19}	8.57	
В	0.58×10^{19}	7.91	3.10×10^{19}	8.41	
C	0.78×10^{19}	8.01	2.60×10^{19}	8.36	
D	1.49×10^{19}	8.18	3.25×10^{19}	8.42	
A-C (Nankai)	5.20×10^{19}	8.56	11.08×10^{19}	8.78	

earthquake (e.g., Johnson & Tebo, 2018; Sherrill & Johnson, 2021). Sherrill and Johnson (2021) estimate that cumulative afterslip following the 1944/46 earthquakes may have released the equivalent of a moment magnitude of $M_{\rm w}$ 8.03.

Figures 5c and 5d show the coupling ratio for the minimum and maximum locked zone moment accumulation rates for Nankai. The minimum and maximum moment accumulation rate coupling maps are much more similar at Nankai than at Cascadia, owing to the smaller uncertainties in boundary locations at Nankai. The locked zones are slightly bigger in the maximum moment map versus the minimum moment map for Nankai, but the shallow creep regions remain roughly the same in both. This demonstrates the utility of seafloor geodetic data in constraining offshore coupling. The two westernmost locked areas at Nankai (NLA1 and NLA2) match well with estimated spatial distributions of coseismic slip from the 1946 Nankai and 1944 Tonankai earthquakes (Figure 1b; e.g., Baba et al., 2002; Murotani et al., 2015; Sagiya & Thatcher, 1999; Sherrill & Johnson, 2021). The estimated epicenters for the 1944 and 1946 earthquakes are also located within and near the locked patch off of Kii Peninsula. Notably, there is very little locking in region B, despite evidence that it slipped during the 1946 earthquake and its location between the 1946 earthquake epicenter and area of maximum slip. Table 3 provides the mean moment accumulation rates and estimated magnitudes for the locked zone and the entire interface for each region at Nankai, as well as estimates for the combined area of the 1944-46 Nankai earthquakes (Regions A-C). The biggest difference between moment accumulation rate and magnitude in the locked zone versus the entire interface is within region B, indicating that while it is not locked, it may still slip during an earthquake, as was inferred for the 1946 earthquake. For the area that ruptured in the 1944/46 earthquakes (Region A-C), we estimate a moment magnitude of M_w 8.56 in the locked zone and M_w 8.78 across the entire interface. This is comparable to other estimates of the combined magnitude of these earthquakes, which range from M8.5–8.56 (e.g., Sagiya & Thatcher, 1999; Sherrill & Johnson, 2021). As mentioned above, it is possible that some of the accumulated moment may be released as afterslip following an earthquake. The data at Nankai were surveyed 1-4 years after the earthquakes so there is some postseismic signal included in the coseismic data (Sagiya & Thatcher, 1999).

Our coupling ratio map (Figure 1b) agrees well with the coupling map of Yokota et al. (2016), especially west of 137°E (regions Z, A, B, and C). In region D, we estimate a larger locked region than Yokota et al. (2016). This is possibly due to the fact that we used more onshore stations in this region than Yokota et al. (2016) and the inherent restriction of our inversion, which requires interseismic slip rates to monotonically increase with depth from the locked zone. However, the locked area in region D has a comparable moment magnitude to estimates of historical Tokai earthquakes of M8.2–8.4 (Hirose et al., 2022).

5.3. Coupling and Slow Earthquakes

Our overall conclusion is that most slow earthquakes occur in the STC and DTC zones at both subduction zones, but at Nankai there are also slow earthquakes within the locked zones. Figure 1 shows the location of slow earthquake observations relative to coupling ratio maps for the median locked moment accumulation rates at Cascadia and Nankai. Most of the slow earthquake observations at Cascadia are located downdip of the locked zone and are within the DTC zone (Figure 1a). At Nankai, the inferred shallow creeping regions match well with locations of VLFEs and shallow SSEs (Figure 1b). These spatial relationships support the suggestion of Takemura et al. (2019) that slow earthquakes occur at regions that are partly coupled and, in particular, in areas with high coupling gradients. For the most part, the ETS zone is contained within the DTC zone at Cascadia and Nankai, and

SHERRILL ET AL. 15 of 21

thus, occurs in regions that are partly coupled. Southern Cascadia is an exception; ETS here occurs mainly in a region of no coupling. This is consistent with the results of Bartlow (2020) which estimates that ETS events in this region release 100% of the accumulated slip deficit. There are two exceptions at Nankai where SSEs have been observed in our inferred locked zone and where careful modeling is needed since there may be non-subduction deformation sources (e.g., volcanoes and crustal faulting) impacting velocities in these regions, Bungo Channel (near 132.25°E, 33°N) and east of Ise Bay (near 137.5°E, 35°N). There have been approximately ten L-SSEs detected in Bungo Channel since 1980, of which four occurred completely within the recording period of the onshore data and only one occurred completely within the recording period of the offshore stations in southern Nankai (e.g., Hirose et al., 2023; Kobayashi & Yamamoto, 2011; Takagi et al., 2019; Yoshioka et al., 2015). The longer durations (~1 year) and recurrence times (~4-6 years) of L-SSEs in Bungo Channel make it difficult to capture an accurate proportion of them in a small snapshot of the interseismic period and, thus, the fault may appear more coupled than it is over the full interseismic period. There are also a few patches, identified by Kano and Kato (2020), off the coast of Shikoku and within and right at the bottom edge of the locked zone. Kano and Kato (2020) interpreted these SSEs (near 133°E, 33°N) to be slow slip invading the locked zone (potentially a manifestation of an updip propagating creep front). These observations, along with the observations of SSEs directly below and slightly overlapping the edge of the locked zone at Cascadia may provide support for their hypothesis.

5.4. Updip Propagating Creep Front

We conclude that there is evidence of updip propagating creep at Cascadia and in some parts of Nankai, which may mean the bottom of the locked zone has moved updip since the last earthquake. Bruhat and Segall (2016) show that in order to fit the velocity data at northern Cascadia, the slip rate gradient needs to be steeper near the bottom edge of the locked zone and gradually taper off to the bottom of the ETS zone. Bruhat and Segall (2017) show that this steep creep rate gradient can be generated if the top edge of the creeping zone propagates into the locked zone where accumulated stress is released by accelerating creep. There are three major implications of a propagating creep front on megathrust earthquake hazard. First, shallowing of the locked zone may be an indication that the previous earthquake ruptured deeper than the present-day bottom edge of the locked zone and therefore rupture estimates based on present-day coupling may be underestimating the size of a future earthquake. Second, a propagating creep front implies that the stressing rate on the locked portion of the interface evolves over time and that the accumulated stress available for rupturing the next earthquake is not simply related to the present-day stressing rate. Third, the stressing rate above the bottom edge of the locked zone increases as the creep front propagates.

Our forward model for creep rate distribution below the locked zone is kinematic, so we are unable to estimate the rate of propagation of the creep front. Bruhat and Segall (2017) utilized fracture mechanics to compute propagation rates between 30 and 120 m/yr, which at a steady rate would amount to 9–36 km of updip propagation over the 300 years since the 1700 earthquake. We find that the inversion results suggest steep creep rate gradients below the locked zone across the entire Cascadia margin, as Bruhat and Segall (2017) found for northern Cascadia. The creep rate gradients are steepest in southern and northern Cascadia (Figure 7) which correlates with areas of increased ETS activity, low Bouguer gravity signatures, and low seismic velocity above the plate interface (Delph et al., 2021), indicating possible links between interseismic creep rate and crustal structure and perhaps the presence of crustal fluids. The steeper creep rate gradients in northern and southern Cascadia also imply lower slip deficit rates in the ETS zone compared to the central section, consistent with higher amounts of cumulative slow slip occurring in the ETS zone over the last 25 years (Bartlow, 2020). Despite evidence for updip propagating creep, all estimates of moment accumulation rates provided in previous sections are assuming no temporal changes in coupling such as updip propagation in creep or other coupling changes such as those found by Materna et al. (2019).

In contrast to Cascadia, our analysis for Nankai suggests gradual creep rate gradients below the locked zone across much of the margin, with f_{shape} values of 2 at four of 10 nodes (Figures 7d–7j, and 7k), and a steeper slip rate gradient beneath eastern Shikoku (Figure 8e and 8f) and Shima Peninsula (Figure 8i). Also in contrast to Cascadia, the creep rate gradients do not correlate with ETS activity rates. The areas in western Shikoku and near Ise Bay that show the highest amounts of cumulative ETS activity have an f_{shape} of only 2 (Kano & Kato, 2020; Nishimura et al., 2013). A physical explanation for the difference in deep creep rate gradients between Cascadia and Nankai needs to be explored in future work. It is possible that the difference can be attributed to the longer

SHERRILL ET AL. 16 of 21

seismic cycle and longer time since the last large earthquake at Cascadia, allowing for more stress accumulation and erosion of the locked zone.

One key difference between our inversion and the work of Bruhat and Segall (2016, 2017) is that we do not utilize vertical velocity data at Cascadia nor at Nankai. Bruhat and Segall (2016) showed that the fit is fairly similar for a constant resistive stress model versus a propagating creep front model when only fitting the horizontal velocity data. Incorporating vertical velocities may improve the resolution of the slip rate gradient profiles (e.g., Bruhat & Segall, 2016; Burgette et al., 2009; Johnson & Tebo, 2018; Liu et al., 2010; Sherrill & Johnson, 2021; Yousefi et al., 2021). However, the vertical velocities will be more sensitive to contributions from viscous mantle flow (e.g., Johnson & Tebo, 2018; Luo & Wang, 2021; Sherrill & Johnson, 2021). Because of the implications a propagating creep front into the locked zone has on seismic hazard, future work will continue exploring the propagating creep front model by jointly inverting the horizontal baseline rate changes and vertical velocities, along with incorporation of viscoelastic cycle models.

6. Conclusions

We developed a non-linear Bayesian inversion that estimates the location of the upper and lower boundaries of the locked zone and the lower boundary of the deep transitional creep zone at Nankai and Cascadia. We identify a locked zone along the entire margin at Cascadia that is widest and deepest in northern Cascadia (near 47.5° N), narrowest in central Cascadia (\sim 20 km wide offshore Oregon), which has a moment accumulation rate that is equivalent to a moment magnitude of M_w 8.71 for a 300-year earthquake cycle and M_w 8.85 for a 500-year earthquake cycle. We estimate that the moment accumulation rate in the locked zone is 48% of the total moment accumulation rate at Cascadia and that some slip outside the locked zone, either coseismic or post-seismic, is required to explain the large moment release observed in the last Cascadia earthquake. We estimate that there are three distinct zones of locking along the Nankai margin (one off of Shikoku, one southeast of Kii peninsula, and one offshore of Shima Peninsula near Ise Bay) with a combined locked zone moment accumulation rate equivalent to a moment magnitude of M_w 8.70. The bottom of the locked zones at Nankai tends to follow the coastline, extending inland some in the western and eastern extents. We estimate the moment accumulation rate in the locked zone accounts for 46% of the total moment accumulation rate with a high moment accumulation rate in the partly coupled region between the 1944 and 1946 earthquakes (between eastern Shikoku and Kii Peninsula).

We utilized a forward model for interseismic slip rate that assumes creep at constant stress above the top of the locked zone to the trench and an approximation to the propagating creep front model of Bruhat and Segall (2017) below the locked zone. We find that the width of the shallow transitional creep zone at Cascadia is uncertain. The top of the locked zone is typically ~9 km but may be as deep as 23 km. The bottom edge of the locked zone is located trenchward of the coastline and is typically no shallower than 9 km in northern and southern Cascadia, however, it may be nonexistent or extend to 20 km depth in central Cascadia. At Nankai, the shallow transitional creep zone fluctuates in width along strike and pinches out the locked zone between the three distinct locked patches. We conclude that much of the Cascadia deep transitional creep zone is characterized by a moderately steep slip rate gradient and that much of the Nankai deep transitional creep zone is characterized by straight to slightly steep slip rate gradients, except beneath eastern Shikoku and Shima peninsula. The moderate to very steep gradients may indicate that the creep front is propagating updip toward the locked zone across the Cascadia margin and beneath Shikoku and Shima peninsula at Nankai. Future work incorporating vertical velocity data, seafloor data in Cascadia, and viscoelastic cycle models may help to place tighter constraints the transitional creep rate profiles. Lastly, we estimate that there may be 0%-40% slip deficit in the ETS zone at Cascadia and 25%-70% slip deficit in the ETS zone at Nankai, indicating that slow slip events are likely not relieving the entire slip budget in the deep transitional creep zone at Cascadia nor Nankai, consistent with prior studies of ETS slip (Bartlow, 2020; Kano & Kato, 2020). We conclude that areas outside the locked zone have the potential to slip significantly coseismically during or postseismically immediately following a megathrust earthquake because there is still considerable moment accumulation in these regions, including the ETS zones at both subduction zones and the region between the two westernmost locked patches at Nankai that is known to have slipped in the 1946 earthquake.

SHERRILL ET AL. 17 of 21

Data Availability Statement

The GNSS derived velocity field for Cascadia is available in Zeng (2022). The MIDAS GNSS velocity field for Nankai is available from the University of Nevada, Reno (Blewitt et al., 2018; http://geodesy.unr.edu/). The offshore seafloor GNSS velocities at Nankai are available as Table S3 in Supporting Information in Yokota et al. (2016). The VLFEs (Asano et al., 2015; Takamura et al., 2022) and tremor (Akuhara et al., 2023; Baba et al., 2023; Obara et al., 2010; Yamashita et al., 2015, 2021) for Nankai were downloaded from "Slow Earthquake Database" (Kano et al., 2018; http://www.solid.eps.s.u-tokyo.ac.jp/~sloweq/). The tremor catalog for Cascadia (Wech, 2021) was downloaded from the Pacific Northwest Seismic Network (https://pnsn.org/tremor/). The Matlab codes used to conduct the inversions presented in this paper are available in a Zenodo public repository (Sherrill et al., 2024a). The principal results of the inversions presented in the figures in this manuscript are available in a Zenodo public repository (Sherrill et al., 2024b).

Acknowledgments

This work was supported by NSF grants EAR-2121631 and EAR-2045291 and USGS grant G20AP00017, and in part by Lilly Endowment, Inc., through its support for the Indiana University Pervasive Technology Institute. We thank Rachel Abercrombie, Kelin Wang, an anonymous reviewer, and our associate editor for their thorough, constructive reviews that improved the manuscript. We thank Michael Hamburger and Gary Pavlis for their detailed and constructive reviews of an early version of this manuscript. We thank Takane Hori for providing useful tools for our modeling efforts at Nankai. We thank Masayuki Kano for providing the short-term slow slip distributions at

References

- Akuhara, T., Yamashita, Y., Sugioka, H., & Shinohara, M. (2023). Locating tectonic tremors with uncertainty estimates: Time-and amplitude-difference optimization, wave propagation-based quality control and Bayesian inversion. *Geophysical Journal International*, 235(3), 2727–2742. https://doi.org/10.1093/gji/ggad387
- Almeida, R., Lindsey, E. O., Bradley, K., Hubbard, J., Mallick, R., & Hill, E. M. (2018). Can the updip Limit of frictional locking on megathrusts Be detected geodetically? Quantifying the effect of stress shadows on near-trench coupling. *Geophysical Research Letters*, 45(10), 4754–4763. https://doi.org/10.1029/2018GL077785
- Annaka, T. (2003). Characteristics of great earthquakes along the Nankai trough based on numerical tsunami simulation. *Journal of Earthquake Engineering*
- Araki, E., Saffer, D. M., Kopf, A. J., Wallace, L. M., Kimura, T., Machida, Y., et al. (2017). Recurring and triggered slow-slip events near the trench at the Nankai Trough subduction megathrust. *Science*, 356(6343), 1157–1160. https://doi.org/10.1126/science.aan3120
- Asano, Y., Obara, K., Matsuzawa, T., Hirose, H., & Ito, Y. (2015). Possible shallow slow slip events in Hyuga-nada, Nankai subduction zone, inferred from migration of very low frequency earthquakes. *Geophysical Research Letters*, 42(2), 331–338. https://doi.org/10.1002/2014.01062165
- Baba, S., Araki, E., Yamamoto, Y., Hori, T., Fujie, G., Nakamura, Y., & Matsumoto, H. (2023). Characteristics of shallow tremor waveforms observed by distributed acoustic sensing using offshore fiber-optic cable at the Nankai Trough, southwest Japan. In *Paper presented at the EGU general assembly Conference Abstracts*.
- Baba, T., Tanioka, Y., Cummins, P. R., & Uhira, K. (2002). The slip distribution of the 1946 Nankai earthquake estimated from tsunami inversion using a new plate model. *Physics of the Earth and Planetary Interiors*, 132(1), 59–73. https://doi.org/10.1016/S0031-9201(02)00044-4
- Bartlow, N. M. (2020). A long-term view of episodic tremor and slip in Cascadia. Geophysical Research Letters, 47(3), e2019GL085303. https://doi.org/10.1029/2019GL085303
- Behr, W. M., & Bürgmann, R. (2021). What's down there? The structures, materials and environment of deep-seated slow slip and tremor. Philosophical Transactions of the Royal Society A, 379(2193), 20200218, https://doi.org/10.1098/rsta.2020.0218
- Blewitt, G., Hammond, W., & Kreemer, C. (2018). Harnessing the GPS data Explosion for Interdisciplinary science. *Eos*, 99. https://doi.org/10. 1029/2018eo104623
- Bruhat, L., & Segall, P. (2016). Coupling on the northern Cascadia subduction zone from geodetic measurements and physics-based models. Journal of Geophysical Research: Solid Earth, 121(11), 8297–8314. https://doi.org/10.1002/2016jb013267
- Bruhat, L., & Segall, P. (2017). Deformation rates in northern Cascadia consistent with slow updip propagation of deep interseismic creep. Geophysical Journal International, 211(1), 427–449. https://doi.org/10.1093/gji/ggx317
- Burgette, R. J., Weldon, R. J., & Schmidt, D. A. (2009). Interseismic uplift rates for western Oregon and along-strike variation in locking on the Cascadia subduction zone. *Journal of Geophysical Research*, 114(B1). https://doi.org/10.1029/2008jb005679
- Bürgmann, R. (2018). The geophysics, geology and mechanics of slow fault slip. Earth and Planetary Science Letters, 495, 112–134. https://doi.org/10.1016/j.epsl.2018.04.062
- Bürgmann, R., Kogan, M. G., Steblov, G. M., Hilley, G., Levin, V. E., & Apel, E. (2005). Interseismic coupling and asperity distribution along the Kamchatka subduction zone. *Journal of Geophysical Research*, 110(B7). https://doi.org/10.1029/2005jb003648
- Chaudhuri, K., & Ghosh, A. (2022). Widespread very low frequency earthquakes (VLFEs) activity offshore Cascadia. Geophysical Research Letters, 49(13), e2022GL097962. https://doi.org/10.1029/2022GL097962
- Chesley, C., LaFemina, P. C., Puskas, C., & Kobayashi, D. (2012). The 1707 Mw8. 7 Hoei earthquake triggered the largest historical eruption of Mt. Fuji. Geophysical Research Letters, 39(24). https://doi.org/10.1029/2012g1053868
- Chlieh, M., Avouac, J. P., Sieh, K., Natawidjaja, D. H., & Galetzka, J. (2008). Heterogeneous coupling of the Sumatran megathrust constrained by geodetic and paleogeodetic measurements. *Journal of Geophysical Research*, 113(B5). https://doi.org/10.1029/2007JB004981
- Delph, J. R., Thomas, A. M., & Levander, A. (2021). Subcretionary tectonics: Linking variability in the expression of subduction along the Cascadia forearc. Earth and Planetary Science Letters, 556, 116724. https://doi.org/10.1016/j.epsl.2020.116724
- Cascadia foreac. Earth and Filaneutry Science Letters, 536, 116724. https://doi.org/10.1016/j.epsl.2020.116724

 DeMets, C., Gordon, R. G., & Argus, D. F. (2010). Geologically current plate motions. Geophysical Journal International, 181(1), 1–80. https://doi.org/10.1111/j.1365-246X.2009.04491.x
- Evans, E. L., Loveless, J. P., & Meade, B. J. (2015). Total variation regularization of geodetically and geologically constrained block models for the Western United States. *Geophysical Journal International*, 202(2), 713–727. https://doi.org/10.1093/gji/ggv164
- Fan, W., Barbour, A. J., McGuire, J. J., Huang, Y., Lin, G., Cochran, E. S., & Okuwaki, R. (2022). Very low frequency earthquakes in between the seismogenic and tremor zones in Cascadia? AGU Advances, 3(2), e2021AV000607. https://doi.org/10.1029/2021AV000607
- Fukuda, J. i., & Johnson, K. M. (2010). Mixed linear—Non-linear inversion of crustal deformation data: Bayesian inference of model, weighting and regularization parameters. *Geophysical Journal International*, 181(3), 1441–1458. https://doi.org/10.1111/j.1365-246x.2010.04564.x
- Furumura, T., Imai, K., & Maeda, T. (2011). A revised tsunami source model for the 1707 Hoei earthquake and simulation of tsunami inundation of Ryujin Lake, Kyushu, Japan. *Journal of Geophysical Research*, 116(B2), B02308. https://doi.org/10.1029/2010jb007918

SHERRILL ET AL. 18 of 21

- Gamerman, D. (1997). Sampling from the posterior distribution in generalized linear mixed models. Statistics and Computing, 7(1), 57–68. https://doi.org/10.1023/a:1018509429360
- Gao, X., & Wang, K. (2017). Rheological separation of the megathrust seismogenic zone and episodic tremor and slip. Nature, 543(7645), 416–419. https://doi.org/10.1038/nature21389
- Ghosh, A., Huesca-Pérez, E., Brodsky, E., & Ito, Y. (2015). Very low frequency earthquakes in Cascadia migrate with tremor. Geophysical Research Letters, 42(9), 3228–3232. https://doi.org/10.1002/2015GL063286
- Gilks, W. R., & Roberts, G. O. (1996). Strategies for improving MCMC. Markov chain Monte Carlo in practice, 6, 89-114.
- Hayes, G. P., Moore, G. L., Portner, D. E., Hearne, M., Flamme, H., Furtney, M., & Smoczyk, G. M. (2018). Slab2, a comprehensive subduction zone geometry model. *Science*, 362(6410), 58–61. https://doi.org/10.1126/science.aat4723
- Herman, M. W., Furlong, K. P., & Govers, R. (2018). The accumulation of slip deficit in subduction zones in the absence of mechanical coupling: Implications for the behavior of megathrust earthquakes. *Journal of Geophysical Research: Solid Earth*, 123(9), 8260–8278. https://doi.org/10.1029/2018jb016336
- Hirose, F., Maeda, K., Fujita, K., & Kobayashi, A. (2022). Simulation of great earthquakes along the Nankai trough: Reproduction of event history, slip areas of the Showa Tonankai and Nankai earthquakes, heterogeneous slip-deficit rates, and long-term slow slip events. *Earth Planets and Space*, 74(1), 131. https://doi.org/10.1186/s40623-022-01689-0
- Hirose, H., Asano, Y., Obara, K., Kimura, T., Matsuzawa, T., Tanaka, S., & Maeda, T. (2010). Slow earthquakes linked along dip in the Nankai subduction zone. Science, 330(6010), 1502. https://doi.org/10.1126/science.1197102
- Hirose, H., Matsushima, T., Tabei, T., & Nishimura, T. (2023). Long-term slow slip events with and without tremor activation in the Bungo Channel and Huyganada, southwest Japan. Earth Planets and Space, 75(77), 77. https://doi.org/10.1186/s40623-023-01833-4
- Hyndman, R. D., McCrory, P. A., Wech, A., Kao, H., & Ague, J. (2015). Cascadia subducting plate fluids channelled to fore-arc mantle corner: ETS and silica deposition. *Journal of Geophysical Research: Solid Earth*, 120(6), 4344–4358. https://doi.org/10.1002/2015jb011920
- Ito, Y., Hino, R., Kido, M., Fujimoto, H., Osada, Y., Inazu, D., et al. (2013). Episodic slow slip events in the Japan subduction zone before the 2011 Tohoku-Oki earthquake. *Tectonophysics*, 600, 14–26. https://doi.org/10.1016/j.tecto.2012.08.022
- Johnson, K. M. (2013). Slip rates and off-fault deformation in Southern California inferred from GPS data and models. *Journal of Geophysical Research: Solid Earth*, 118(10), 5643–5664. https://doi.org/10.1002/jgrb.50365
- Johnson, K. M., & Fukuda, J. i. (2010). New methods for estimating the spatial distribution of locked asperities and stress-driven interseismic creep on faults with application to the San Francisco Bay Area, California. *Journal of Geophysical Research*, 115(B12). https://doi.org/10.1029/2010/ib/007703
- Johnson, K. M., Murray, J. R., & Wespestad, C. (2022). Creep rate models for the 2023 US National seismic hazard model: Physically constrained inversions for the distribution of creep on California faults. Seismological Research Letters, 93(6), 3151–3169. https://doi.org/10.1785/ 0220220186
- Johnson, K. M., & Tebo, D. (2018). Capturing 50 Years of postseismic mantle flow at Nankai subduction zone. *Journal of Geophysical Research:* Solid Earth, 123(11), 10091–10106. https://doi.org/10.1029/2018jb016345
- Johnson, K. M., Wallace, L. M., Maurer, J., Hamling, I., Williams, C., Rollins, C., et al. (2024). Inverting geodetic strain rates for slip deficit rate in complex deforming zones: An application to the New Zealand plate boundary. *Journal of Geophysical Research: Solid Earth*, 129(3), e2023JB027565. https://doi.org/10.1029/2023JB027565
- Kano, M., Aso, N., Matsuzawa, T., Ide, S., Annoura, S., Arai, R., et al. (2018). Development of a slow earthquake database. Seismological Research Letters, 89(4), 1566–1575. https://doi.org/10.1785/0220180021
- Kano, M., & Kato, A. (2020). Detailed spatial slip distribution for short-term slow slip events along the Nankai subduction zone, southwest Japan. Journal of Geophysical Research: Solid Earth, 125(7), e2020JB019613. https://doi.org/10.1029/2020jb019613
- Kano, M., Kato, A., & Obara, K. (2019). Episodic tremor and slip silently invades strongly locked megathrust in the Nankai Trough. Scientific Reports, 9(1), 9270. https://doi.org/10.1038/s41598-019-45781-0
- Kobayashi, A. (2017). Objective detection of long-term slow slip events along the Nankai Trough using GNSS data (1996–2016). Earth Planets and Space, 69(1), 171. https://doi.org/10.1186/s40623-017-0755-7
- Kobayashi, A., & Yamamoto, T. (2011). Repetitive long-term slow slip events beneath the Bungo Channel, southwestern Japan, identified from leveling and sea level data from 1979 to 2008. *Journal of Geophysical Research*, 116(B4), B04406. https://doi.org/10.1029/2010JB007822
- Li, S., Wang, K., Wang, Y., Jiang, Y., & Dosso, S. E. (2018). Geodetically inferred locking state of the Cascadia megathrust based on a viscoelastic Earth model. *Journal of Geophysical Research: Solid Earth*, 123(9), 8056–8072. https://doi.org/10.1029/2018jb015620
- Lindsey, E. O., Mallick, R., Hubbard, J. A., Bradley, K. E., Almeida, R. V., Moore, J. D., et al. (2021). Slip rate deficit and earthquake potential on shallow megathrusts. *Nature Geoscience*, 14(5), 321–326. https://doi.org/10.1038/s41561-021-00736-x
- Liu, Z., Owen, S., Dong, D., Lundgren, P., Webb, F., Hetland, E., & Simons, M. (2010). Estimation of interplate coupling in the Nankai trough, Japan using GPS data from 1996 to 2006. *Geophysical Journal International*. https://doi.org/10.1111/j.1365-246X.2010.04600.x
- Loveless, J. P., & Meade, B. J. (2010). Geodetic imaging of plate motions, slip rates, and partitioning of deformation in Japan. *Journal of Geophysical Research*, 115(B2). https://doi.org/10.1029/2008jb006248
- Luo, H., & Wang, K. (2021). Postseismic geodetic signature of cold forearc mantle in subduction zones. Nature Geoscience, 14(2), 104–109. https://doi.org/10.1038/s41561-020-00679-9
- MacKay, D. J. (2003). Information theory, inference and learning algorithms. Cambridge university press.
- Materna, K., Bartlow, N., Wech, A., Williams, C., & Bürgmann, R. (2019). Dynamically triggered changes of plate interface coupling in southern Cascadia. Geophysical Research Letters, 46(22), 12890–12899. https://doi.org/10.1029/2019GL084395
- Matsuzawa, T., Hirose, H., Shibazaki, B., & Obara, K. (2010). Modeling short- and long-term slow slip events in the seismic cycles of large subduction earthquakes. *Journal of Geophysical Research*, 115(B12). https://doi.org/10.1029/2010jb007566
- Mavrommatis, A. P., Segall, P., Uchida, N., & Johnson, K. M. (2015). Long-term acceleration of aseismic slip preceding the Mw 9 Tohoku-oki earthquake: Constraints from repeating earthquakes. *Geophysical Research Letters*, 42(22), 9717–9725. https://doi.org/10.1002/2015GL066069
- Melgar, D., Sahakian, V. J., & Thomas, A. M. (2022). Deep coseismic slip in the Cascadia megathrust can be consistent with coastal subsidence. Geophysical Research Letters, 49(3), e2021GL097404. https://doi.org/10.1029/2021g1097404
- Metois, M., Vigny, C., & Socquet, A. (2016). Interseismic coupling, megathrust earthquakes and seismic swarms along the Chilean subduction zone (38–18 S). *Pure and Applied Geophysics*, 173(5), 1431–1449. https://doi.org/10.1007/s00024-016-1280-5
- Metropolis, N., Rosenbluth, A. W., Rosenbluth, M. N., Teller, A. H., & Teller, E. (1953). Equation of state calculations by fast computing machines. *The journal of chemical physics*, 21(6), 1087–1092. https://doi.org/10.1063/1.1699114
- Moreno, M., Rosenau, M., & Oncken, O. (2010). 2010 Maule earthquake slip correlates with pre-seismic locking of Andean subduction zone. Nature, 467(7312), 198–202. https://doi.org/10.1038/nature09349

SHERRILL ET AL. 19 of 21

- Murotani, S., Shimazaki, K., & Koketsu, K. (2015). Rupture process of the 1946 Nankai earthquake estimated using seismic waveforms and geodetic data. *Journal of Geophysical Research: Solid Earth*, 120(8), 5677–5692. https://doi.org/10.1002/2014jb011676
- Nakanishi, A., Takahashi, N., Yamamoto, Y., Takahashi, T., Citak, S. O., Nakamura, T., et al. (2018). Three-dimensional plate geometry and P-wave velocity models of the subduction zone in SW Japan: Implications for seismogenesis. Geology and Tectonics of Subduction Zones: A Tribute to Gaku Kimura, 69–86. https://doi.org/10.1130/2018.2534(04)
- Nishimura, T., Matsuzawa, T., & Obara, K. (2013). Detection of short-term slow slip events along the Nankai Trough, southwest Japan, using GNSS data. *Journal of Geophysical Research: Solid Earth*, 118(6), 3112–3125. https://doi.org/10.1002/jgrb.50222
- Nocquet, J. M., Jarrin, P., Vallée, M., Mothes, P. A., Grandin, R., Rolandone, F., et al. (2017). Supercycle at the Ecuadorian subduction zone revealed after the 2016 Pedernales earthquake. *Nature Geoscience*, 10(2), 145–149. https://doi.org/10.1038/ngeo2864
- Nuyen, C. P., & Schmidt, D. A. (2021). Filling the gap in Cascadia: The Emergence of low-amplitude long-term slow slip. Geochemistry, Geophysics, Geosystems, 22(3), e2020GC009477. https://doi.org/10.1029/2020GC009477
- Obara, K. (2002). Nonvolcanic deep tremor associated with subduction in southwest Japan. Science, 296(5573), 1679–1681. https://doi.org/10.1126/science.1070378
- Obara, K., Tanaka, S., Maeda, T., & Matsuzawa, T. (2010). Depth-dependent activity of non-volcanic tremor in southwest Japan. *Geophysical Research Letters*, 37(13), n/a-n-a. https://doi.org/10.1029/2010gl043679
- Okada, Y. (1992). Internal deformation due to shear and tensile faults in a half-space. Bulletin of the Seismological Society of America, 82(2), 1018–1040. https://doi.org/10.1785/bssa0820021018
- Peng, Z., & Gomberg, J. (2010). An integrated perspective of the continuum between earthquakes and slow-slip phenomena. *Nature Geoscience*, 3(9), 599–607, https://doi.org/10.1038/ngeo940
- Petersen, M. D., Shumway, A. M., Powers, P. M., Mueller, C. S., Moschetti, M. P., Frankel, A. D., et al. (2020). The 2018 update of the US National seismic hazard model: Overview of model and implications. *Earthquake Spectra*, 36(1), 5–41. https://doi.org/10.1177/8755293019878199
- Pollitz, F., & Evans, E. (2017). Implications of the earthquake cycle for inferring fault locking on the Cascadia megathrust. Geophysical Journal International, 209(1), 167–185.
- Ramos, M. D., Huang, Y., Ulrich, T., Li, D., Gabriel, A. A., & Thomas, A. M. (2021). Assessing margin-wide rupture behaviors along the Cascadia megathrust with 3-D dynamic rupture simulations. *Journal of Geophysical Research: Solid Earth*, 126(7), e2021JB022005. https://doi.org/10.1029/2021jb022005
- Rogers, G., & Dragert, H. (2003). Episodic tremor and slip on the Cascadia subduction zone: The Chatter of Silent slip. Science, 300(5627), 1942–1943. https://doi.org/10.1126/science.1084783
- Ruiz, S., Aden-Antoniow, F., Baez, J., Otarola, C., Potin, B., del Campo, F., et al. (2017). Nucleation phase and dynamic inversion of the Mw 6.9 Valparaíso 2017 earthquake in Central Chile. *Geophysical Research Letters*, 44(20), 10290–10297. https://doi.org/10.1002/2017gl075675
- Sagiya, T., & Thatcher, W. (1999). Coseismic slip resolution along a plate boundary megathrust: The Nankai Trough, southwest Japan. *Journal of Geophysical Research*, 104(B1), 1111–1129. https://doi.org/10.1029/98jb02644
- Saito, T., & Noda, A. (2022). Mechanically coupled areas on the plate interface in the Nankai Trough, Japan and a possible seismic and aseismic rupture scenario for megathrust earthquakes. *Journal of Geophysical Research: Solid Earth*, 127(8), e2022JB023992. https://doi.org/10.1029/2022jb023992
- Satake, K., Wang, K., & Atwater, B. F. (2003). Fault slip and seismic moment of the 1700 Cascadia earthquake inferred from Japanese tsunami descriptions. *Journal of Geophysical Research*, 108(B11). https://doi.org/10.1029/2003jb002521
- Savage, J. C. (1983). A dislocation model of strain accumulation and release at a subduction zone. *Journal of Geophysical Research*, 88(B6), 4984–4996. https://doi.org/10.1029/JB088iB06p04984
- Schmalzle, G. M., McCaffrey, R., & Creager, K. C. (2014). Central Cascadia subduction zone creep. *Geochemistry, Geophysics, Geosystems*, 15(4), 1515–1532. https://doi.org/10.1002/2013gc005172
- Segall, P., & Bradley, A. M. (2012). Slow-slip evolves into megathrust earthquakes in 2D numerical simulations. *Geophysical Research Letters*, 39(18). https://doi.org/10.1029/2012gl052811
- Shelly, D. R., Beroza, G. C., Ide, S., & Nakamula, S. (2006). Low-frequency earthquakes in Shikoku, Japan, and their relationship to episodic tremor and slip. *Nature*, 442(7099), 188–191. https://doi.org/10.1038/nature04931
- Sherrill, E., & Johnson, K. (2021). New insights into the slip budget at Nankai: An iterative approach to estimate coseismic slip and afterslip. Journal of Geophysical Research: Solid Earth, 126(2), 2020JB020833, https://doi.org/10.1029/2020jb020833
- Sherrill, E. M., Johnson, K. M., & Jackson, N. M. (2024a). Boundary inversion codes used in Sherrill et al. (2024) [Software]. Zenodo. https://doi.org/10.5281/zenodo.10979734
- Sherrill, E. M., Johnson, K. M., & Jackson, N. M. (2024b). Result files for boundary inversion of Sherrill et al. (2024) [Data set]. Zenodo. https://doi.org/10.5281/zenodo.10978768
- Takagi, R., Obara, K., & Maeda, T. (2016). Slow slip event within a gap between tremor and locked zones in the Nankai subduction zone. Geophysical Research Letters, 43(3), 1066–1074. https://doi.org/10.1002/2015gl066987
- Takagi, R., Uchida, N., & Obara, K. (2019). Along-strike variation and migration of long-term slow slip events in the western Nankai subduction zone, Japan. *Journal of Geophysical Research: Solid Earth*, 124(4), 3853–3880. https://doi.org/10.1029/2018JB016738
- Takemura, S., Noda, A., Kubota, T., Asano, Y., Matsuzawa, T., & Shiomi, K. (2019). Migrations and clusters of shallow very low frequency earthquakes in the regions surrounding shear stress accumulation Peaks along the Nankai trough. *Geophysical Research Letters*, 46(21), 11830–11840. https://doi.org/10.1029/2019GL084666
- Takemura, S., Obara, K., Shiomi, K., & Baba, S. (2022). Spatiotemporal variations of shallow very low frequency earthquake activity southeast off the Kii Peninsula, along the Nankai Trough, Japan. *Journal of Geophysical Research: Solid Earth*, 127(3), e2021JB023073. https://doi.org/10.1029/2021jb023073
- Uchida, N., Iinuma, T., Nadeau, R. M., Bürgmann, R., & Hino, R. (2016). Periodic slow slip triggers megathrust zone earthquakes in northeastern Japan. Science, 351(6272), 488–492. https://doi.org/10.1126/science.aad3108
- Wang, K., & Dixon, T. (2004). "Coupling" semantics and science in earthquake research. Eos, Transactions American Geophysical Union, 85(18), 180. https://doi.org/10.1029/2004eo180005
- Wang, K., Wells, R., Mazzotti, S., Hyndman, R. D., & Sagiya, T. (2003). A revised dislocation model of interseismic deformation of the Cascadia subduction zone. *Journal of Geophysical Research*, 108(B1). https://doi.org/10.1029/2001jb001227
- Wang, P.-L., Engelhart, S. E., Wang, K., Hawkes, A. D., Horton, B. P., Nelson, A. R., & Witter, R. C. (2013). Heterogeneous rupture in the great Cascadia earthquake of 1700 inferred from coastal subsidence estimates. *Journal of Geophysical Research: Solid Earth*, 118(5), 2460–2473. https://doi.org/10.1002/jgrb.50101

SHERRILL ET AL. 20 of 21

- Wech, A. G. (2021). Cataloging tectonic tremor Energy Radiation in the Cascadia subduction zone. *Journal of Geophysical Research: Solid Earth*, 126(10), e2021JB022523. https://doi.org/10.1029/2021JB022523
- Wech, A. G., & Creager, K. C. (2011). A continuum of stress, strength and slip in the Cascadia subduction zone. *Nature Geoscience*, 4(9), 624–628. https://doi.org/10.1038/ngeo1215
- Wirth, E. A., & Frankel, A. D. (2019). Impact of down-dip rupture Limit and high-stress Drop Subevents on coseismic Land-level change during Cascadia megathrust earthquakes. Bulletin of the Seismological Society of America, 109(6), 2187–2197. https://doi.org/10.1785/0120190043
- Yamashita, Y., Shinohara, M., & Yamada, T. (2021). Shallow tectonic tremor activities in Hyuga-nada, Nankai subduction zone, based on long-term broadband ocean bottom seismic observations. Earth Planets and Space, 73, 1–11. https://doi.org/10.1186/s40623-021-01533-x
- Yamashita, Y., Yakiwara, H., Asano, Y., Shimizu, H., Uchida, K., Hirano, S., et al. (2015). Migrating tremor off southern Kyushu as evidence for slow slip of a shallow subduction interface. *Science*, 348(6235), 676–679. https://doi.org/10.1126/science.aaa4242
- Yokota, Y., & Ishikawa, T. (2020). Shallow slow slip events along the Nankai Trough detected by GNSS-A. *Science Advances*, 6(3), eaay5786. https://doi.org/10.1126/sciadv.aay5786
- Yokota, Y., Ishikawa, T., Watanabe, S., Tashiro, T., & Asada, A. (2016). Seafloor geodetic constraints on interplate coupling of the Nankai Trough megathrust zone. *Nature*, 534(7607), 374–377. https://doi.org/10.1038/nature17632
- Yoshioka, S., Matsuoka, Y., & Ide, S. (2015). Spatiotemporal slip distributions of three long-term slow slip events beneath the Bungo Channel, southwest Japan, inferred from inversion analyses of GPS data. *Geophysical Journal International*, 201(3), 1427–1455. https://doi.org/10.1093/gji/ggv022
- Yousefi, M., Milne, G. A., & Latychev, K. (2021). Glacial isostatic adjustment of the Pacific coast of north America: The influence of lateral earth structure. *Geophysical Journal International*, 226(1), 91–113. https://doi.org/10.1093/gji/ggab053
- Zeng, Y. (2022). GPS velocity field of the western United States for the 2023 National seismic hazard model update. Seismological Research Letters, 93(6), 3121–3134. https://doi.org/10.1785/0220220180
- Zeng, Y., & Shen, Z. K. (2017). A fault-based model for crustal deformation in the western United States based on a combined inversion of GPS and geologic inputs. *Bulletin of the Seismological Society of America*, 107(6), 2597–2612. https://doi.org/10.1785/0120150362

SHERRILL ET AL. 21 of 21